Cell Reports

Article

# Selective ablation of primary and paracrine senescent cells by targeting iron dyshomeostasis

## Graphical abstract

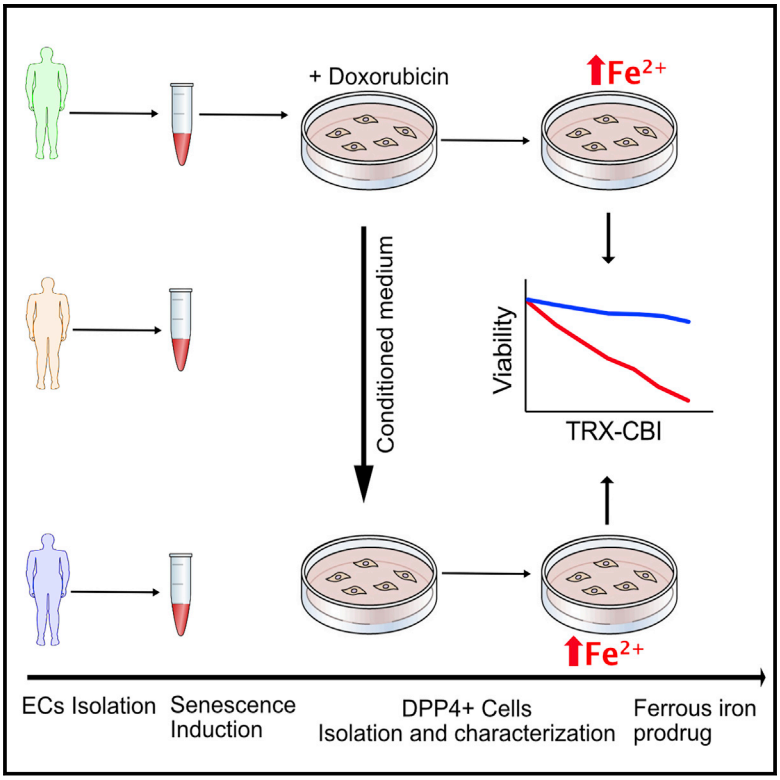


## Highlights

- DPP4$^+$ paracrine SCs are distinct from primary SCs
- DPP4$^+$ paracrine SCs are less susceptible to current senolytics
- Ferroptosis induction is a senolytic approach for primary and paracrine SCs
- Ferrous iron-activated prodrug represents a broad-spectrum senolytics approach


## Authors

Tesfahun Dessale Admasu, Kristie Kim, Michael Rae, ..., Adam R. Renslo, Alexandra Stolzing, Amit Sharma

## Correspondence

dessaletesfahun@gmail.com (T.D.A.), amit.sharma@sens.org (A.S.)



## In brief

Admasu et al. used DPP4 to isolate and enrich paracrine SCs. They showed that paracrine SCs are resistant to previously reported senolytic drugs. They identified ferroptosis induction and ferrous iron-activated prodrug as a broad-spectrum senolytic approach to kill multiple types of primary and paracrine SCs.


Admasu et al., 2023, Cell Reports *42*, 112058
February 28, 2023 
https://doi.org/10.1016/j.celrep.2023.112058

CellPress

Cell Reports

CellPress
OPEN ACCESS

Article

# Selective ablation of primary and paracrine senescent cells by targeting iron dyshomeostasis

Tesfahun Dessale Admasu,[1,5,*] Kristie Kim,[1] Michael Rae,[1] Roberto Avelar,[2] Ryan L. Gonciarz,[3] Abdelhadi Rebbaa,[1] João Pedro de Magalhães,[2] Adam R. Renslo,[3] Alexandra Stolzing,[4] and Amit Sharma[1,*]

[1]SENS Research Foundation, Mountain View, CA 94041, USA
[2]Integrative Genomics of Ageing Group, Institute of Ageing and Chronic Disease, University of Liverpool, Liverpool, UK
[3]Department of Pharmaceutical Chemistry, University of California, San Francisco, San Francisco, CA, USA
[4]Loughborough University, Centre for Biological Engineering, School of Mechanical, Electrical and Manufacturing Engineering, Epinal Way, Loughborough LE113TU, UK
[5]Lead contact
*Correspondence: dessaletesfahun@gmail.com (T.D.A.), amit.sharma@sens.org (A.S.)
https://doi.org/10.1016/j.celrep.2023.112058

## SUMMARY

Senescent cells can spread the senescent phenotype to other cells by secreting senescence-associated secretory phenotype factors. The resulting paracrine senescent cells make a significant contribution to the burden of senescent cell accumulation with age. Previous efforts made to characterize paracrine senescence are unreliable due to analyses being based on mixed populations of senescent and non-senescent cells. Here, we use dipeptidyl peptidase-4 (DPP4) as a surface maker to isolate senescent cells from mixed populations. Using this technique, we enrich the percentage of paracrine senescence from 40% to 85%. We then use this enriched culture to characterize DPP4$^{+}$ primary and paracrine senescent cells. We observe ferroptosis dysregulation and ferrous iron accumulation as a common phenomenon in both primary and paracrine senescent cells. Finally, we identify ferroptosis induction and ferrous iron-activatable prodrug as a broad-spectrum senolytic approach to ablate multiple types of primary and paracrine senescent cells.

## INTRODUCTION

In the United States, people over the age of 65 are expected to comprise nearly a quarter of the population by 2060.[1] This aging population is expected to put an unprecedented burden on the healthcare system as the link between aging and several chronic diseases has been well documented.[2,3] Thus, it is a priority to develop interventions targeting the biological aging process to medically bend the rising curve of age-related morbidity.[2,4,5]

Cellular senescence was originally discovered by Hayflick et al. as a cell state of permanent cell-cycle arrest.[6] The accumulation of senescent cells (SCs) in various tissues results in dysfunction,[7–9] which is thought to be primarily driven by their secretion of a unique mix of proinflammatory factors termed the senescence-associated secretory phenotype (SASP), which can contribute to an age-related local or systemic inflammation (also called "inflammaging").[10–12] Drugs that selectively destroy SCs (senolytics) have been shown to extend healthy lifespan[8,13] and to delay, ameliorate, or in some respects reverse multiple age-related diseases in animal models and human studies, which supports a causal link between SC burden and various age-related diseases. Thus, elimination of SCs offers great promise in the development of therapeutic interventions for several age-related pathologies.[14,15]

However, SCs have been shown to have substantial heterogeneity. For instance, senescence caused by different stresses such as replicative arrest, expression of oncogenes, and genotoxic stress results in differences in molecular signature.[16] Furthermore, the senescent phenotype can vary depending on the tissue of origin.[17,18] Hence, more in-depth understanding of the molecular regulatory pathways of cellular senescence is still an ongoing endeavor. In this context, the main topic of the present study is paracrine senescence, which is one of the most recently discovered and least understood forms of senescence.[19–23]

Most studies on SCs have been conducted in so-called "primary" SCs, (S), which have been induced into permanent cell-cycle arrest upon exposure to insults that can be inflicted by laboratory techniques such as exposure to DNA damaging agents, extended replication, telomere loss or damage, mitochondrial dysfunction, or oncogene activation. The more recently discovered paracrine senescent cells (PSs) instead enter a senescent state upon prolonged exposure to SASP factors produced by primary SCs.[19] Paracrine senescence has not only been demonstrated to occur in cell culture but has also been shown to drive the accumulation of SCs and subsequent functional defects of aged mice *in vivo*.[13,21,24,25]

However, comparative studies of S and PSs have been hampered due to the lack of precise model systems.[19] In previous *in vitro* studies, when paracrine senescence was induced by exposing non-senescent cells (NSs) to SASP-containing conditioned medium (CM) from S, only less than 40% of treated cells

had undergone senescence, resulting in a heterogeneous population of cells.[21–23]

In this study, we sought to characterize the phenotypic properties of S and PSs by isolating and enriching PSs based on surface expression of DPP4 (dipeptidyl peptidase-4), a previously reported SC surface marker.[26] We used patient-derived primary endothelial cells (ECs) induced to paracrine senescence with CM collected from doxorubicin-treated primary SCs. We then isolated $DPP4^+$ SCs and were able to achieve a robust enrichment of PSs from 40% to 85% based on multiple senescence markers. Using this improved enrichment system, we discovered that $DPP4^+$ paracrine SCs ($PS^{DPP4+}$) engage prosurvival pathways that are distinct from those on which $DPP4^+$ primary SCs ($S^{DPP4+}$) rely and are also relatively resistant to killing by senolytic drugs previously identified to be effective against primary SCs. Given that SCs accumulate ferrous iron (Fe(II), also known as labile iron), we sought to test a Fe(II)-targeting strategy in which Fenton reaction of a prodrug was coupled to release of drug payload. Renslo and co-workers previously showed[27] that the tumor-activated prodrug TRX-CBI (comprising a trioxolane-based [TRX] sensor of Fe(II) conjugated to a cytotoxic cyclopropylbenzindoline [CBI] payload) demonstrated selective toxicity in Fe(II)-rich cancer cells. Here, we used a single stereoisomeric form of TRX-CBI (which was prepared from the *trans*-(R,R)-TRX alcohol intermediate as described in Blank et al.[28]) to target cytotoxic CBI to SCs. We demonstrated that treatment with TRX-CBI triggers significant senolysis of both $PS^{DPP4+}$ and $S^{DPP4+}$, with negligible cytotoxicity toward NSs. Based on our results, we propose Fe(II)-based targeting of SCs with ferroptosis inducers or iron-activated drug conjugates as broad-spectrum senolytic agents.

## RESULTS

### SCs express DPP4 on their surface

It was recently reported that ECs are particularly susceptible to age-associated senescence, with the majority of $p16^{high}$ SCs in mice found to be ECs.[29] We therefore used primary patient-derived ECs (artery and vein iliac ECs from three young donors aged 21, 22, and 23) as a model to study paracrine senescence. We induced primary senescence with doxorubicin treatment, and paracrine senescence was induced by treating cells with CM collected from doxorubicin-treated cells (Figure S1A). Our results showed that 90% of doxorubicin-treated cells (S) have senescence-associated beta-galactosidase (SA β Gal) activity vs. only 40% of cells treated with CM collected from S. By contrast, cells treated with vehicle (NSs) or CM collected from non-senescent cells (NSCM) had significantly lower SA β Gal activity (Figures S1B and S1D). Further, 90% of S were observed to have two or more γH2AX foci per nucleus, whereas only 40% of PSs had two or more foci per nucleus (Figures S1C and S1E). Our results also showed that while nearly all NSs or NSCM-treated cells had HMGB1 (high mobility group box 1) localized in the nucleus, about 60% of S and 20% of PSs had HMGB1 localized both to the nucleus and the cytosol. (Figures S1C and S1F). Finally, only 10% of S or PSs were proliferating (EdU positive), indicating that most SCs had undergone proliferation arrest (Figure S1G). However, it should be noted that EdU staining did not distinguish between senescent and quiescent cells, the latter of which might be caused due to low serum medium in PSs.

DPP4 has been reported as a surface marker of senescent fibroblasts.[26] Our immunofluorescence (IF) results confirmed the expression of DPP4 on the surface of senescent human fibroblasts (IMR90) (Figures S1H and S1I) and human mesenchymal stem cells (MSCs) (Figures S1K and S1L). These results were confirmed by flow cytometric analysis to determine the surface expression of DPP4 in live SCs. In both IMR90 and MSCs, over 90% of SCs expressed DPP4 on their surface vs. only 42% and 26% of the NSs respectively (Figures S1J and S1M). We then determined surface expression of DPP4 in S (Figures S1N–S1P) and paracrine senescent (Figures S1Q–S1S) ECs isolated from three donors, qualitatively by IF and quantitatively by flow cytometry. On average, 75% of primary SCs and 60% of PSs from three donors expressed DPP4 on their surface, whereas less than 5% of NSs and NSCM-treated cells were DPP4 positive (Figure S1T).

### Isolation of live SCs using DPP4 as a surface marker

Consistent with previously published data,[20,21] we found that less than 40% of cells exposed to CM from primary SCs become paracrine senescent (Figure S1). To isolate and enrich PSs from this heterogeneous pool of CM-treated cells, we sorted $DPP4^+$ and $DPP4^-$ cells using a magnetic separation column (see STAR Methods section) and analyzed for multiple senescence markers. Our assay confirmed that 82.5% of $PS^{DPP4+}$ stained positive for SA β Gal, which was comparable to $DPP4^+$ primary SCs ($S^{DPP4+}$) (Figures 1A, S2A–S2D, and S2I). Enrichment of PSs was further confirmed by quantitation of γH2AX foci, showing that 82% of $PS^{DPP4+}$ have two or more foci per nucleus (Figures 1B, S2E–S2H, and S2J). Further, 72% of $PS^{DPP4+}$ lost HMGB1 from the nucleus (Figures 1C and S2E–S2H). Fewer than 10% of the NSs and NSCM-treated cells were positive for the aforementioned senescence markers. There was no statistically significant difference between $S^{DPP4+}$ and $PS^{DPP4+}$ in any of the makers tested above. Quantitative real-time PCR also revealed a significantly higher expression of $p16^{Ink4a}$ and $p21^{Cip1}$ and a decrease in the expression of *lmnb1* in $PS^{DPP4+}$ and $S^{DPP4+}$ cells compared with NSs and NSCM-treated cells (Figures 1D–1F). Our results also demonstrated significantly higher levels of IL-6 and IL-8 secretion in both $S^{DPP4+}$ and $PS^{DPP4+}$ compared with NSs or NSCM-treated cells (Figure 1G).

To determine whether DPP4 can be used to isolate SCs irrespective of senescence induction method and cell type of origin, we induced primary and paracrine senescence in ECs by exposure to either ionizing radiation or CM collected from irradiated cells, respectively. By applying the same method, we isolated $DPP4^+$ SCs and managed to increase the percentage of PSs to 83.5% based on SA β Gal and γH2AX foci counting (Figures S2K and S2L). We then moved to a different cell type, IMR90 fibroblasts, and induced primary senescence by doxorubicin treatment. In IMR90 cells, isolation of SCs based on DPP4 expression resulted in 75% paracrine senescence based on SA β Gal and γH2AX foci counting (Figures S2M and S2N). Taken together, these data showed that PSs can be isolated and enriched based on DPP4 surface expression (Figure 1J). Of note, our SA β Gal and γH2AX IF assays showed that less than 20%

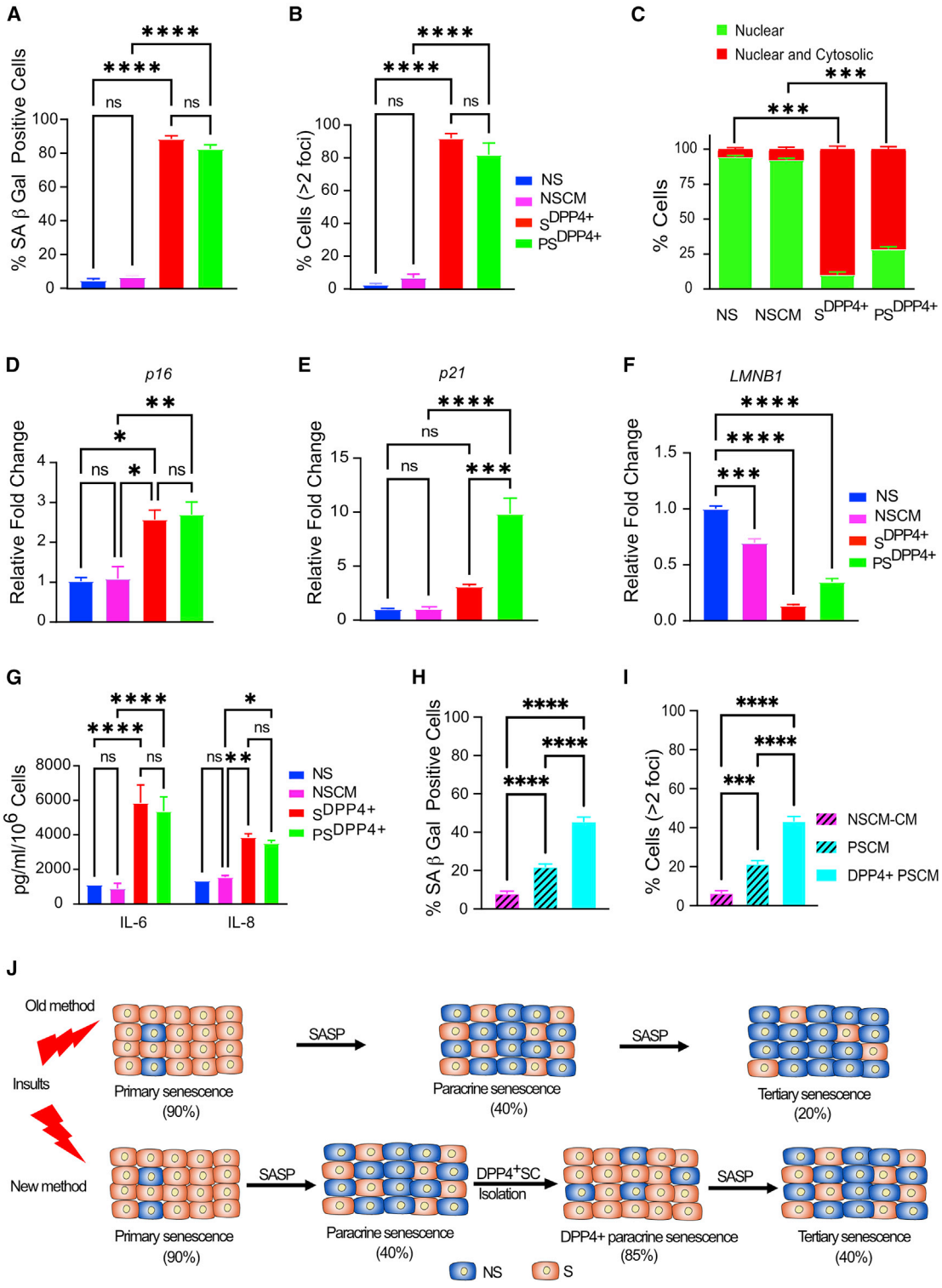


**Figure 1. Isolation of live SCs using DPP4 as a surface marker**

(A) Percent of SA β Gal positive cells in DPP4$^{+}$ isolated primary and paracrine senescent ECs ($S^{DPP4+}$ and $PS^{DPP4+}$) from three donors.

(B) Quantification of γH2AX foci in $S^{DPP4+}$ and $PS^{DPP4+}$. Cells with two or more foci per nucleus were defined as SCs.

(C) HMGB1 relocalizes in $S^{DPP4+}$ and $PS^{DPP4+}$. Percentage of cells expressing HMGB1 in the nucleus and nucleus + cytosol was scored.

(D and E) mRNA expression of $p16^{Ink4a}$ and $p21^{Cip1}$ was determined by qRT-PCR in $S^{DPP4+}$ and $PS^{DPP4+}$.

*(legend continued on next page)*

of DPP4$^-$ cells are senescent (vs. 80%–85% in DPP4$^+$ cells) (Figures S2O and S2P).

## PS$^{DPP4+}$ cells spread senescence as tertiary senescence

A previous investigation reported that SASP factors from primary SCs can induce senescence in about half of the cells exposed to the CM, whereas SASP factors from PSs induce senescence in only 10%–16% cells.[21] However, this study was carried out using mixed cultures containing PSs and NSs, likely diluting their SASP and thus their potential to induce senescence. Another study showed blunting of SASP due to repression through NOTCH signaling as a reason for a weak induction of tertiary senescence.[30] Unlike in that study, we focused on the effect of paracrine senescence without the influence of physical contact between cells on the induction of senescence. Our results demonstrated upregulation of several SASP factors known to induce senescence such as *il-6*, *il-8*, *igfbp3*, and *tgfβ* in enriched PS$^{DPP4+}$ (Figure 3D; see also Admasu et al.[19]). Further, secreted levels of IL-6 and IL-8 by PS$^{DPP4+}$ were comparable to S$^{DPP4+}$ (Figure 1G). Therefore, we investigated whether SASP factors secreted by PS$^{DPP4+}$ further spread senescence as tertiary senescence. Results demonstrated that CM from unenriched PSs induced senescence in only 20% of treated cells as measured by SA β Gal assay and γH2AX foci (Figures 1H and 1I). By contrast, CM collected from PS$^{DPP4+}$ induced senescence in 40% of treated cells (Figures 1H and 1I). These results suggest that PS$^{DPP4+}$ can spread senescence as tertiary senescence (Figure 1J).

## PS$^{DPP4+}$ are refractory to senolytic drugs effective against S$^{DPP4+}$

In our efforts to characterize PS$^{DPP4+}$, we measured the expression of anti-apoptotic BCL family proteins that are known to be constitutively upregulated in SCs.[31] Our western blot analysis revealed elevated levels of BCL-2, BCL-xL, and BCL-w in S$^{DPP4+}$ compared with NSs (Figure 2A). By contrast, while we observed a similar increase in BCL-xL and BCL-w expression in PS$^{DPP4+}$, BCL-2 protein expression was substantially lower compared with S$^{DPP4+}$. As BCL-2 antagonists are often used to selectively kill SCs, we tested the effect of members of this class of senolytic drugs on S$^{DPP4+}$ and PS$^{DPP4+}$. To this end, isolated S$^{DPP4+}$ and PS$^{DPP4+}$ were treated with senolytic drugs for 72 h unless otherwise specified (Figure 2B). Our results demonstrated that treatment with ABT-199, a specific inhibitor of BCL-2, for 24 h, killed S$^{DPP4+}$ in a dose-dependent manner, with 50% killing at its previously reported optimal dose (5 μM), while only 25% of PS$^{DPP4+}$ were killed at this concentration (Figure 2C). Further, with increasing concentration, the drug was observed to be toxic to NSs as well (Figure S3A). Surprisingly, ABT-263, a pan-BCL-2 inhibitor, was also less effective in killing PS$^{DPP4+}$ compared with S$^{DPP4+}$. At its previously reported optimal dose (0.5 μM), ABT-263 killed 45% of S$^{DPP4+}$ and only 20% of PS$^{DPP4+}$ cells (Figure 2D), whereas a higher dose of 1 μM killed up to 50% of PS$^{DPP4+}$ (Figure S3B). We also tested the senolytic effect of quercetin and its combination with dasatinib (D+Q). 5 μM of quercetin killed 40% of S$^{DPP4+}$ and 37% of PS$^{DPP4+}$, with less than 5% cytotoxicity toward NSs and NSCM-treated cells (Figures 2E and S3C). On the other hand, D+Q combination exhibited poor selectivity for SCs, killing 74% of S$^{DPP4+}$ and 66% of PS$^{DPP4+}$ but also 42% of NSs and 50% of NSCM-treated ECs (Figures 2F and S3D).

## Transcriptome profile of S$^{DPP4+}$ and PS$^{DPP4+}$

We performed RNA-seq analysis on S$^{DPP4+}$ and PS$^{DPP4+}$ isolated and enriched senescent ECs from three young donors. After stringent filtration ($|LFC| \geq 1$ and P adj. $< 0.05$), we found 1,240 genes in S$^{DPP4+}$ compared with NSs and 1,316 genes in PS$^{DPP4+}$ compared with NSCM-treated cells as differentially expressed genes (DEGs) (Table S1). Of 1,316 DEGs of PS$^{DPP4+}$, 945 (72%) were uniquely expressed in PS$^{DPP4+}$ (Figure S4A). 2D principal-component analysis (PCA) (Figure 3A) showed the variance (PC1) caused by the differences in the tissue of origin (S$^{DPP4+}$ and PS$^{DPP4+}$ samples from artery [one donor] vs. vein [two donors]), followed by the variance (PC2) caused by mode of senescence induction (i.e., primary vs. paracrine). Analysis at the donor level (Table S2) also demonstrated that S$^{DPP4+}$ and PS$^{DPP4+}$ are distinct from each other (Figures 3B, S4B, and S4C). Further, heatmap analysis showed that PS$^{DPP4+}$ were well separated from S$^{DPP4+}$ and clustered together in all three donors (Figures 3C and S4D–S4F).

We then categorized the DEGs based on biological process, molecular function, and cellular component gene ontology (GO) term categories using PANTHER classification system.[32] Overall, S$^{DPP4+}$ and PS$^{DPP4+}$ showed similar trends in all three categories (Figures S4G and S4H). The top biological processes enriched were biological regulation followed by metabolic process, whereas membrane was the top cellular component, and protein binding was the top molecular function enriched in both S$^{DPP4+}$ and PS$^{DPP4+}$. We further analyzed our data for functional enrichment using WebGestalt (web-based gene set analysis toolkit)[33] and found several senescence-associated pathways such as p53, protein secretion, apoptosis, and mTORC1 signaling and proinflammatory pathways such as interferon alpha (IFN-α) and interferon gamma (IFN-γ) to be among the top enriched terms of upregulated genes in both S$^{DPP4+}$ and PS$^{DPP4+}$ (Figures S5A and S5B). We validated the top DEGs by qRT-PCR and confirmed that *gdf7*, *wnt5b*, *igfbp5*, and *cst1* were upregulated in both S$^{DPP4+}$ and PS$^{DPP4+}$ (Figures 3E–3H), whereas *igfbp3*, *pappa2*, *epha7*, and *tnc* were significantly upregulated in PS$^{DPP4+}$ compared with S$^{DPP4+}$ (Figures 3I–3L). We

(F) Same as in (E) for LMNB1.
(G) IL-6 and IL-8 secretion was measured by ELISA in CM from S$^{DPP4+}$ and PS$^{DPP4+}$ in three donors.
(H) Tertiary senescence: percent of SA β Gal-positive cells in cells treated with CM collected from PSs and PS$^{DPP4+}$.
(I) Tertiary senescence: percent of cells with two or more γH2AX foci per nucleus in cells treated with CM collected from PSs and PS$^{DPP4+}$.
(J) Comparison of previous method and our method of comparing primary and paracrine SCs. See also Figures S1 and S2 (n = 9 in three donors). Values were presented as mean ± SEM. Comparison was made with one-way ANOVA. *p < 0.05, **p < 0.01, ***p < 0.001, ****p < 0.0001.

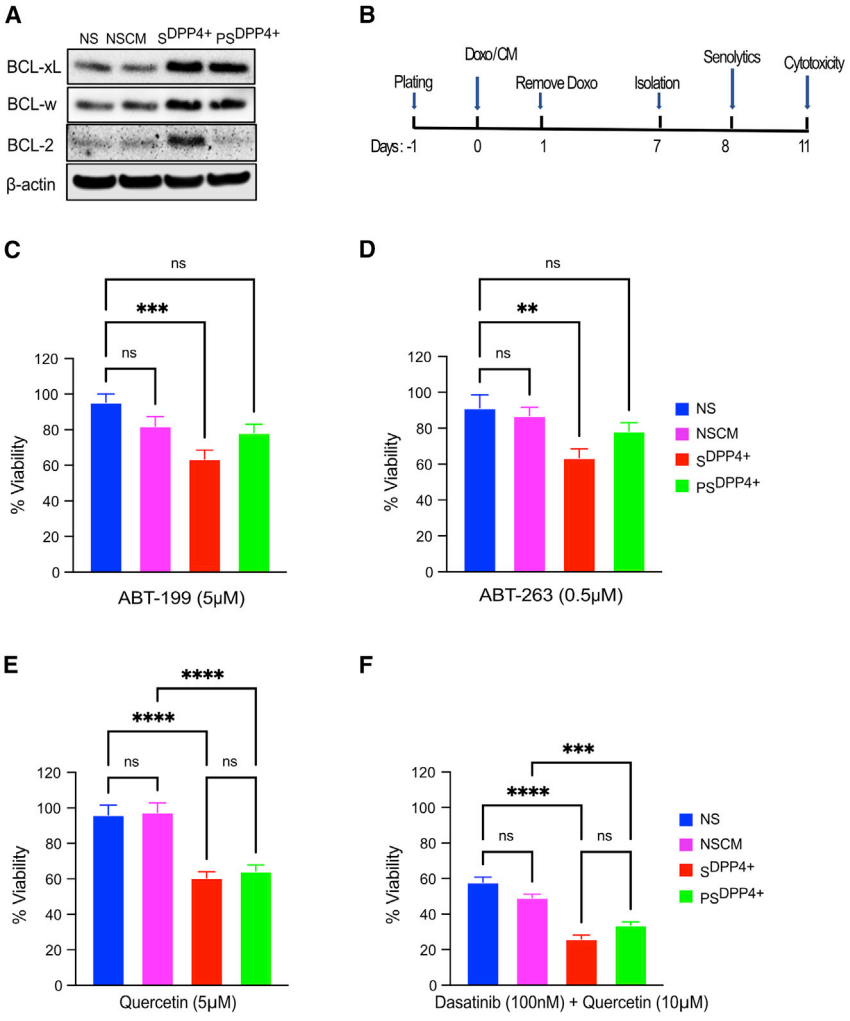


**Figure 2. $PS^{DPP4+}$ are refractory to senolytic drugs effective against $S^{DPP4+}$**

(A) Expression levels of prosurvival BCL-2 family proteins in $S^{DPP4+}$ and $PS^{DPP4+}$.

(B) Experimental design for (C)–(F) and other senolytic studies.

(C) ABT-199 has senolytic activity in $S^{DPP4+}$ but not in $PS^{DPP4+}$. Quantification of viable cells 24 h after treatment. See Figure S3A for dose response.

(D) ABT-263 has senolytic activity in $S^{DPP4+}$ but limited effect in $PS^{DPP4+}$. Quantification of viable cells 72 h after treatment. See Figure S3B for dose response.

(E) Quercetin has senolytic activity in both $S^{DPP4+}$ and $PS^{DPP4+}$. Quantification of viable cells 72 h after treatment. See Figure S3C for dose response.

(F) D+Q combination is non-selectively toxic toward SCs and NSs. Quantification of viable cells 72 h after treatment with 10 μM Q and 100 nM concentrations of D. See Figure S3D for dose response. (n = 9 in three donors). Comparison was made with one-way ANOVA. Error bars represent mean ± SEM. *p < 0.05, **p < 0.01, ***p < 0.001, ****p < 0.0001.

tested several genes by qRT-PCR but did not find any marker that was unique to either $S^{DPP4+}$ or $PS^{DPP4+}$.

We next compared the SASP composition of $S^{DPP4+}$ and $PS^{DPP4+}$ based on SASP factors reported in SASPAtlas, Acosta et al., and Wiley et al.[21,34,35] Several of the SASP factors reported for primary SCs were differentially expressed in our $S^{DPP4+}$ and $PS^{DPP4+}$ RNA-seq data (Table S3). Our qRT-PCR data confirmed the upregulation of several classical SASP factors such as *il6*, *il8*, *il1α* (Figure 3D), *tgf-β* (Figure 4E), *gdf7* (Figure 3E), and *igfbp3* (Figure 3I). We also observed increased expression of chemokines such as *ccl2*, *ccl5*, and *cxcl9* in both $S^{DPP4+}$ and $PS^{DPP4+}$ (Figure 3D).

Finally, we compared our RNA-seq data of $PS^{DPP4+}$ with previously published data on secondary SCs reported by Acosta et al.[21] and Teo et al.[20] Comparing these two datasets with our RNA-seq data of $PS^{DPP4+}$, we found high heterogeneity among the secondary SCs, with only one gene (*abi3bp*) conserved among the three reports (Figure S5C). Expression of *abi3bp* has been shown to trigger senescence through the p21 pathway in thyroid tumor cells.[36] Further comparison of the three datasets as presented by circos plot (Figure S5D) and enrichment network analysis (Figure S5E) revealed that there is a high overlap at the GO term enrichment. However, it should be noted that the three datasets are different regarding the cell types tested, senescence induction methods, and analysis techniques that are described elsewhere.[19]

## $S^{DPP4+}$ and $PS^{DPP4+}$ accumulate high levels of ferrous iron

Metallothioneins (*mt*) and solute carrier protein (*slc*)-related genes were among the top DEGs in $PS^{DPP4+}$ and $S^{DPP4+}$ (Figures 4A and 4B). Both *mts* and *slcs* are known to regulate iron transportation[37] and homeostasis.[38] Additionally, our RNA-seq data revealed differential expression of several iron metabolism-related genes in $S^{DPP4+}$ and $PS^{DPP4+}$ (Figure 4C and Table S4). Quantitative RT-PCR in both $S^{DPP4+}$ and $PS^{DPP4+}$ samples confirmed significantly elevated levels of *slc7a11* and *tgfbr1* and downregulation of *tfrc* and *mt1g* (Figures 4D–4G). We further confirmed that iron metabolism regulatory proteins such as the iron importer transferrin receptor and iron exporter ferroportin-1 (FPN) were downregulated in $S^{DPP4+}$ and $PS^{DPP4+}$ (Figure 4H), further indicating iron dyshomeostasis in SCs. However, we did not observe a change in ferritin expression level (Figure 4H).

We next determined the total iron content in $S^{DPP4+}$ and $PS^{DPP4+}$ cells by inductively coupled plasma optical-emission spectroscopy (ICP). The result demonstrated significantly elevated levels of total iron in $S^{DPP4+}$ and $PS^{DPP4+}$ compared with NS controls (Figure 4I). We also measured the redox-active Fe(II) (labile iron) content in $S^{DPP4+}$ and $PS^{DPP4+}$ with SiRhoNox-1 probe-based flow analysis (Figures 4J, S6A, and S6B) and imaging (Figures S6C and S6D). Both $S^{DPP4+}$ and $PS^{DPP4+}$ ECs have

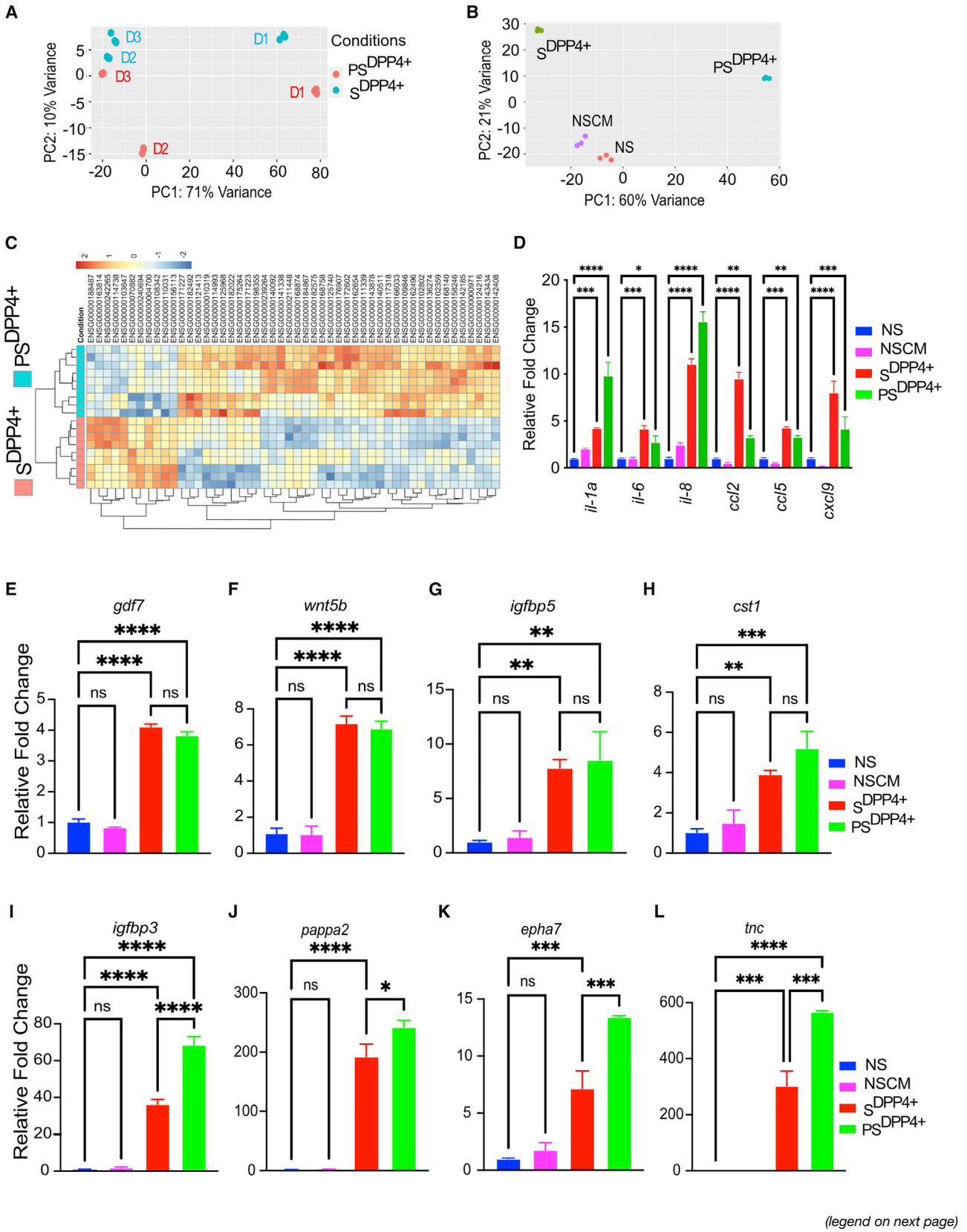


*(legend on next page)*

significantly elevated levels of Fe(II) compared with their respective NS controls for all three donors we tested. 80% of $S^{DPP4+}$ and $PS^{DPP4+}$ cells were positive for Fe(II) in this assay vs. 30% of the NSs and NSCM-treated controls (Figure 4J).

## Ferroptosis is dysregulated in $S^{DPP4+}$ and $PS^{DPP4+}$ cells

Pathway analysis of DEGs of $PS^{DPP4+}$ revealed that genes responsible for the enrichment of the top three pathways (e.g., *il-1α*, *il-1β*, *tgfβ*, and *notch*) are genes known to have an interaction with each other and to be involved in paracrine senescence induction (Figures 5A and 5B). The other top enriched pathways in this analysis were autophagy, ferroptosis, and cholesterol synthesis (Figure 5A). In the cholesterol synthesis pathway, squalene synthase is the target of FIN56, a drug known to induce ferroptosis in cancer cells.[39] Autophagy-mediated degradation of damaged mitochondria, aggregated proteins, and excess peroxisomes contribute to ferroptosis by increasing iron overload. In agreement, our RNA-seq data also showed differential regulation of several ferroptosis-related genes in $S^{DPP4+}$ and $PS^{DPP4+}$ (Figure 5C and Table S5). We further confirmed this observation by qRT-PCR and showed the upregulation of several genes known to regulate ferroptosis (*slc7a11*, *nfe2l2*, *chac1*, and *ptgs2*) in $S^{DPP4+}$ and $PS^{DPP4+}$ (Figures 5D and 5E). Importantly, the expression of *acsl4 gene* was significantly higher in $S^{DPP4+}$ and $PS^{DPP4+}$ (Figure 5F). ACSL4 mediates ferroptosis through the generation of precursors to bioactive lipid mediators.[40,41] In agreement with this, we observed high levels of lipid peroxidation in $S^{DPP4+}$ and $PS^{DPP4+}$ as determined by Bodipy C11 staining (Figures S6E and S6F), which was further supported by elevated levels of malondialdehyde (a final product of lipid peroxidation) in $S^{DPP4+}$ and $PS^{DPP4+}$ (Figure S6G).

We next asked if ferroptosis inducers can selectively ablate SCs. We treated $S^{DPP4+}$ and $PS^{DPP4+}$ ECs with two ferroptosis inducers, RSL3 and FIN56.[39] Cell viability was determined by real-time cytotoxicity assay (xCELLigence). Results showed that RSL3 treatment did not have selective cytotoxicity toward $S^{DPP4+}$ and $PS^{DPP4+}$ (Figure S6H), whereas FIN56 selectively reduced viability of both $S^{DPP4+}$ and $PS^{DPP4+}$ ECs in a dose-dependent manner (Figure 6A). Treatment with 0.5 μM of FIN56 reduced viability of $S^{DPP4+}$ (doxorubicin treated) and $PS^{DPP4+}$ ECs by 43% and 41.5% respectively. In contrast, we observed limited loss in viability of NSs and NSCM-treated cells treated with FIN56 (6.5%) (Figure 6A). Next, to determine if the senolytic effect of FIN56 was independent of the cell type of origin, we tested it in doxorubicin-treated fibroblasts (IMR90) and their derived PSs. FIN56 (0.5 μM) killed 40% of $S^{DPP4+}$ and 33% of $PS^{DPP4+}$ fibroblasts with limited effect on NSs and NSCM-treated cells (Figure 6B). The senolytic activity of FIN56 was further confirmed in etoposide-treated ECs and their derived PSs (Figure S6I). Finally, to rule out the possibility that the senolytic activity of FIN56 was restricted to SCs expressing DPP4, we confirmed its effect on primary SCs without DPP4-based isolation (Figure S6J) and in $DPP4^-$ SCs (Figure S6K), and again, we observed similar senolytic activity across $DPP4^+$ and $DPP4^-$ SCs.

## FIN56 kills SCs through ferroptosis

We measured the gene expression of two previously reported targets of FIN56, *gpx4* and *fdft1*, before and after treatment. SCs have modestly higher levels of *gpx4* and *fdft1* gene expression compared with NSs, and FIN56 treatment significantly increased the expression of *fdft1* and tended to decrease *gpx4* expression (Figure 6C). FIN56-treated SCs have higher level of *ptgs2*, which is known to execute ferroptosis, compared with untreated SCs (Figure 6C). To investigate the mechanism of cell death, we co-treated SCs with FIN56 and various cell death pathway inhibitors, including ferroptosis inhibitor ferrostatin-1 (Fer-1), iron chelator deferiprone (DFP), and pan-caspase inhibitor z-VAD-fmk. SCs co-treated with pan-caspase inhibitor z-VAD-fmk were still sensitive to FIN56, suggesting that FIN56 is unlikely to kill targets by apoptosis (Figure 6D). By contrast, co-treatment with DFP significantly reduced FIN56-mediated cytotoxicity of SCs (Figure 6E). Further, cotreatment with Fer-1 also significantly reduced the cytotoxicity of FIN56 in SCs (Figure 6F). These data showed that the increases in intracellular Fe(II) and ferroptosis are necessary for the senolytic activity of FIN56.

Finally, to independently confirm the susceptibility of SCs to ferroptosis, we transfected S IMR90 cells with small interfering RNAs (siRNAs) directed against GPX4 (siGPX4) or non-target siRNA (siCtrl). The efficacy of knockdown was confirmed at the mRNA and protein levels 48 and 72 h later, respectively (Figures 6G and 6H). SCs were significantly more sensitive to GPX4 knockdown compared with NSs as determined by crystal violet staining (Figure S7A). siGPX4 killed 44% of S IMR90 cells with less than 5% cytotoxicity in NSs (Figure 6I).

## Ferrous iron-activatable prodrug as a senolytic approach

Given that SCs have elevated levels of Fe(II) (Figure 4J), we hypothesized that a Fe(II)-activatable prodrug would be preferentially processed by SCs, resulting in their selective killing (Figure 7G). To test this hypothesis, we used the previously described CBI conjugated with TRX (TRX-CBI), which has been shown to selectively kill cancer cells with high Fe(II) loads.[27] First, we evaluated the effect of the naked CBI cytotoxin or its TRX-masked conjugate (TRX-CBI) on the viability of NSs. While

**Figure 3. Transcriptome profile of $S^{DPP4+}$ and $PS^{DPP4+}$**

(A) 2D PCA of $S^{DPP4+}$, $PS^{DPP4+}$, NSs, and NSCM-treated cells from three donors.

(B) 2D PCA of $S^{DPP4+}$, $PS^{DPP4+}$, NSs, and NSCM-treated cells from one donor. See Figures S4B and S4C for other donors.

(C) Heatmap of the top 50 DEGs for $S^{DPP4+}$ and $PS^{DPP4+}$ from three donors. Heat maps indicate the averages of six experiments (n = 3 technical replicates for three donors). See also Figure S4.

(D) Classical SASP factors expression in $S^{DPP4+}$ and $PS^{DPP4+}$.

(E–L) RNA-seq confirmation by qRT-PCR. mRNAs encoding for *GDF7* (E), *WNT5B* (F), *IGFBP5* (G), *CST1* (H), *IGFBP3* (I), *PAPPA2* (J), *EPHA7* (K), and *TNC* (L) genes were measured by qPCR. Comparison was made with one-way ANOVA. Error bars represent mean ± SEM. *p < 0.05, **p < 0.01, ***p < 0.001, ****p < 0.0001.

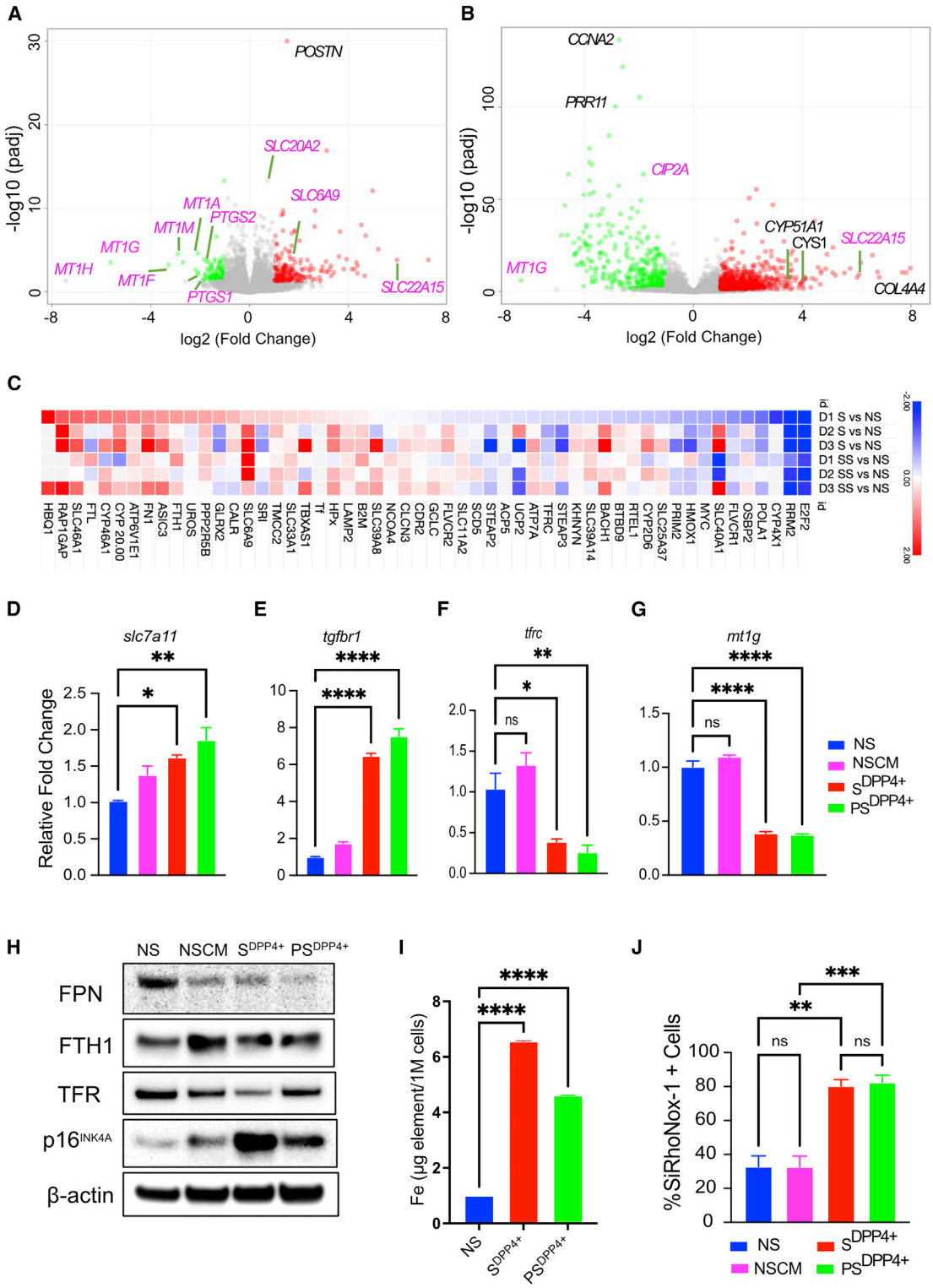


**Figure 4. $S^{DPP4+}$ and $PS^{DPP4+}$ have high levels of ferrous iron accumulation**

(A) Volcano plot for DEGs of $PS^{DPP4+}$.

(B) Volcano plot for DEGs of $S^{DPP4+}$.

(C) Heatmap of iron metabolism-related genes from three donors.

*(legend continued on next page)*

treatment with naked CBI was toxic to NSs, TRX-CBI had negligible cytotoxicity, confirming the masking effect of the TRX moiety (Figure S7B). By contrast, when we treated $S^{DPP4+}$ and $PS^{DPP4+}$ ECs with TRX-CBI, we observed preferential ablation of both $S^{DPP4+}$ and $PS^{DPP4+}$ with negligible effect on NSs and NSCM-treated cells (Figure 7A). Optimally, treatment with 20 nM of TRX-CBI for 72 h killed 87% of $S^{DPP4+}$ and 78% of $PS^{DPP4+}$ ECs with less than 15% cytotoxicity toward NSs and NSCM-treated ECs. To determine the effect of treatment over longer duration, we measured cytotoxicity for 4 days and found that by day 4, TRX-CBI (20 nM) killed 100% of $S^{DPP4+}$ and $PS^{DPP4+}$ ECs with 30% cytotoxicity on NSs and NSCM-treated cells (Figure 7B).

To determine the effect of TRX-CBI in multiple modes of senescence, we tested its effect in etoposide-treated ECs and their derived $PS^{DPP4+}$ cells. TRX-CBI selectively killed both etoposide-treated $S^{DPP4+}$ and their derived $PS^{DPP4+}$ (Figure 7D). To understand whether the prodrug's senolytic effect was restricted to ECs or also observed in other cell types, we induced senescence in IMR90 fibroblasts by doxorubicin treatment. TRX-CBI selectively killed $S^{DPP4+}$ and their $PS^{DPP4+}$ IMR90 cells over NSs and NSCM-treated cells (Figure S7C). Furthermore, TRX-CBI killed 80% of etoposide-treated senescent IMR90 cells (Figure S7D). These data suggest that senolytic effect of TRX-CBI was not restricted by the cell type or senescence induction method. Additionally, this senolytic activity was not limited to $DPP4^+$ SCs, as TRX-CBI killed primary SCs without isolation based on DPP4 (Figure 7C). To further confirm this, we also showed that TRX-CBI effectively killed both $DPP4^+$ and $DPP4^-$ SCs (Figure 7E).

Finally, we showed that treatment with TRX-CBI induced apoptosis in SCs as determined by annexin V and propidium iodide staining (Figure S7E), and the selective death of SCs was significantly prevented with the pan-caspase inhibitor Z-VAD-FMK (Figure 7F). In summary, our data suggest that TRX-CBI selectively triggers apoptosis of SCs in an Fe(II)-dependent manner (Figure 7G). Based on our results, we propose that the aberrant iron metabolism in SCs is a broadly exploitable senolytic target. Ferroptosis inducers and Fe(II)-activated prodrugs merit further investigation as broad-spectrum senolytic agents.

## DISCUSSION

The molecular biology of cellular senescence has opened the possibility of exploiting the differential vulnerabilities of SCs compared with healthy cells for the development of a new class of longevity therapeutics against aging and age-related disorders.[42,43] However, the significant heterogeneity among SCs based on cell type of origin or senescence induction method[16,17,19] suggests the need to develop senolytics that either have a broader therapeutic efficacy or that can target recalcitrant SCs.

In this context, paracrine senescence is the least understood type of senescence. Even though there have been previous efforts to characterize PSs, the fact that only a subset of cells exposed to SASP factors become senescent means that previous experimental protocols were compromised, with mixed cell populations dominated by NSs labeled as PSs.[19,21] We were able to circumvent this major methodological issue by isolating and enriching PSs using the previously characterized SC surface marker DPP4.[26]

SASP factors are indispensable for both juxtacrine and paracrine forms of secondary senescence.[20,21] Acosta et al. reported that even though CM from S induces paracrine senescence in dividing cells in culture, the CM from PSs could not induce tertiary senescence.[21] This inability could be due to either the dilution of SASP components (due to the mixed population of PSs and NSs) or a difference in SASP composition between S and PSs.[19] Contrary to the prediction of the second hypothesis, we showed that $PS^{DPP4+}$ secrete prototypical SASP factors IL-6 and IL-8 at levels comparable to $S^{DPP4+}$ (Figure 1). These factors are known to induce senescence.[19] Instead, our results supported the first explanation by showing that CM from $PS^{DPP4+}$ can induce tertiary senescence at rates comparable to the degree of paracrine senescence induction by the CM of primary SCs.

SCs are known to resist apoptotic clearance, but the prosurvival mechanisms that the SCs engage are distinct depending on the mechanism of senescence induction and cell type of origin.[31,44,45] Thus, these differences confer differential susceptibilities to various senolytics.[31,46] Here, we showed that $S^{DPP4+}$and $PS^{DPP4+}$ rely on distinct prosurvival mechanisms and have differential susceptibility toward current senolytics (Figure 2).

SCs had been previously reported to be resistant to ferroptosis.[47] In fact, elevated expression of p21, one of the two main drivers of cell-cycle arrest in SCs, has been reported to confer resistance to ferroptosis,[48] However, the downstream mechanisms of this recalcitrance remains to be investigated. Cells become sensitive to ferroptosis when they have high levels of Fe(II), oxidizable ω-6 polyunsaturated fats, and a defect in the repair system of lipid peroxidation.[49] High iron levels have previously been reported in SCs and in aged mouse liver with high SC burden, without specifying the redox activity of this iron.[47] We found that $S^{DPP4+}$ and $PS^{DPP4+}$ accumulate significant amounts of Fe(II) as indicated with SiRhoNox-1 (Figure 4). Another group has similarly reported that SiRhoNox-1 labels several SC models with high selectivity.[50]

Several mechanisms have been implicated for the elevated iron levels in SCs, including impaired ferritinophagy, upregulated iron uptake, and inactivated iron efflux via ferroportin.[47]

(D–G) Confirmation of mRNA expression of iron metabolism-related genes. mRNAs encoding *SLC7A11* (D), *TGFBR1* (E), *TFRC* (F), and *MT1G* (G) genes were measured by qPCR.
(H) Western blot for analysis of iron metabolism-related proteins.
(I) Total iron content in $S^{DPP4+}$ and $PS^{DPP4+}$ cells.
(J) Quantification of SiRhoNox-$1^+$ cells from three donors. Comparison was made with one-way ANOVA. Error bars represent mean ± SEM. *$p < 0.05$, **$p < 0.01$, ***$p < 0.001$, ****$p < 0.0001$.

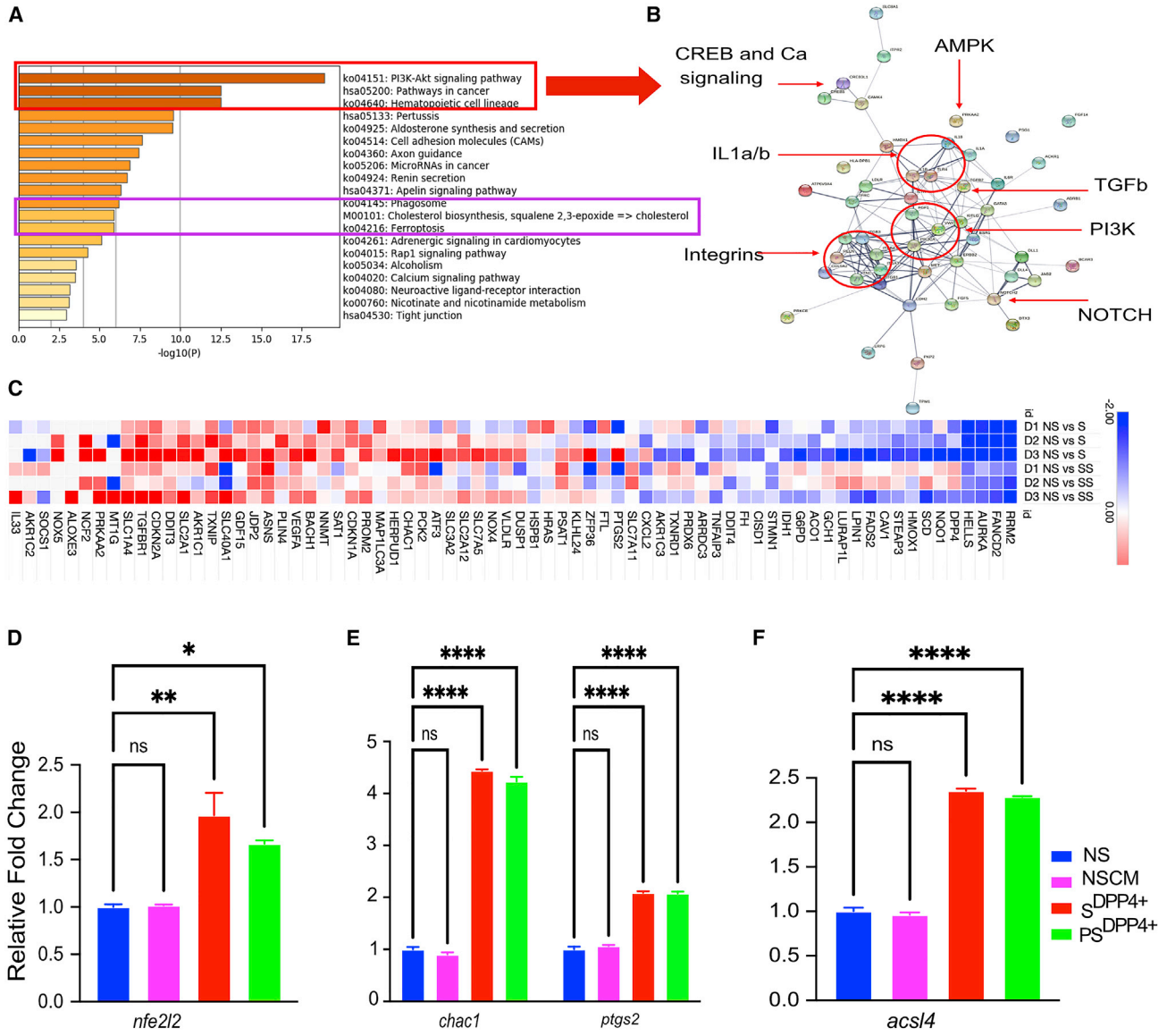


**Figure 5. Ferroptosis is dysregulated in $S^{DPP4+}$ and $PS^{DPP4+}$**

(A) Pathway analysis for DEGs of $PS^{DPP4+}$.

(B) Protein-protein networks of interaction for genes responsible for the top three pathways in (A).

(C) Heatmap of ferroptosis-related genes.

(D–F) Confirmation of mRNA expression of ferroptosis-related genes. mRNAs encoding for *NFE2L2* (D), *CHAC1* and *PTGS2* (E), and *ACSL4* (F) genes were measured by qRT-PCR. Comparison was made with one-way ANOVA. Error bars represent mean ± SEM. *p < 0.05, **p < 0.01, ***p < 0.001, ****p < 0.0001.

Studies testing these hypotheses have reported contrasting results,[51,52] possibly implying an incomplete or inconsistent engagement of homeostatic compensatory mechanisms. Regardless, the elevated levels of Fe(II) are permissive for ferroptosis.

In addition to elevated levels of Fe(II), SCs also have high expression of *NFE2L2*, which activates the cellular antioxidant response to membrane damage during ferroptosis.[53,54] We also found increased expression of *CHAC1* and *PTGS2* in both types of SCs, and both these genes are consistently upregulated in (and in the case of *CHAC1*, required for) ferroptosis.[53] Thus, SCs appear to be primed for ferroptosis, yet we and others find them recalcitrant to it, suggesting that some other mechanism(s) is responsible for the basal resistance of SCs to ferroptosis.

FIN56 reduced the viability of $S^{DPP4+}$and $PS^{DPP4+}$ irrespective of the cell type of origin (Figure 5). FIN56 promotes degradation of GPX4 and depletion of the antioxidant $CoQ_{10}$,[39] which together compromise the antioxidant defense of the cells. FIN56 may also enhance iron bioavailability by triggering lysosomal membrane permeability.[55] The inability of FIN56 to kill SCs in the presence of iron chelator DFP or ferroptosis inhibitor

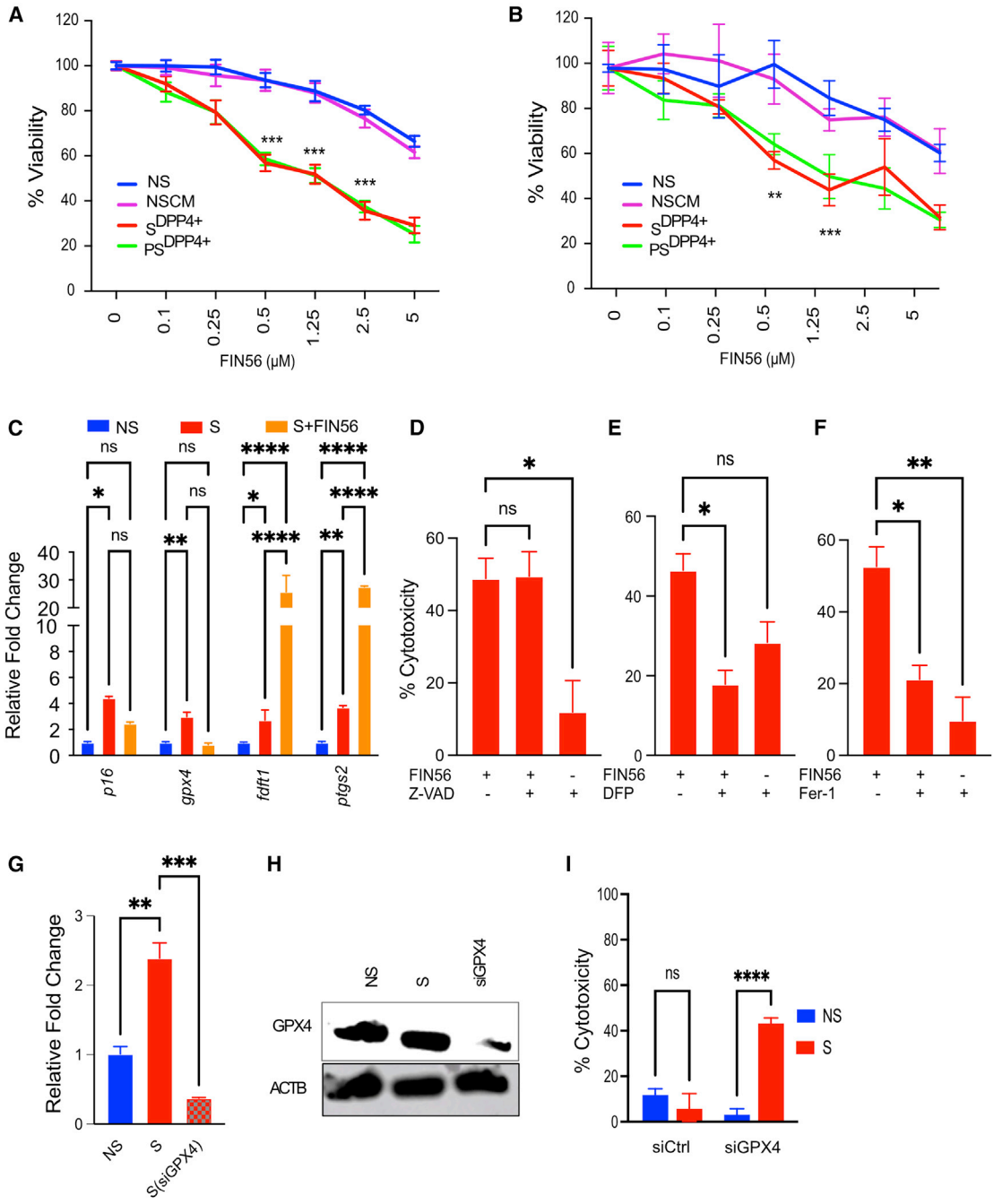


**Figure 6. FIN56 induces ferroptosis in $S^{DPP4+}$ and $PS^{DPP4+}$ cells**

(A) Cytotoxicity of FIN56 in $S^{DPP4+}$ and $PS^{DPP4+}$ ECs 72 h after treatment (n = 9, in three donors).

(B) Cytotoxicity of FIN56 in $S^{DPP4+}$ and $PS^{DPP4+}$ IMR90 fibroblasts 72 h after treatment (n = 3).

(C) mRNA expression of *p16* and ferroptosis-related genes (*GPX4*, *FDFT1*, and *PTGS2*) before and after FIN56 treatment.

(D–F) Quantification of viable $S^{DPP4+}$ ECs (doxorubicin treated) 72 h after treatment with FIN56 alone or FIN56 + z-vad-fmk (D), FIN56 + DFP (E), and FIN56 + Fer-1 (F). Viability was determined by xCELLigence real-time cell analysis (RTCA).

(G) Confirmation of GPX4 knockdown by siGPX4 at the mRNA level.

(H) Confirmation of GPX4 knockdown by siGPX4 at the protein level.

(I) Cytotoxic effect of siGPX4 in senescent IMR90 cells was determined by crystal violet assay. Comparison was made with one-way ANOVA. Error bars represent mean ± SEM. *p < 0.05, **p < 0.01, ***p < 0.001, ****p < 0.0001.

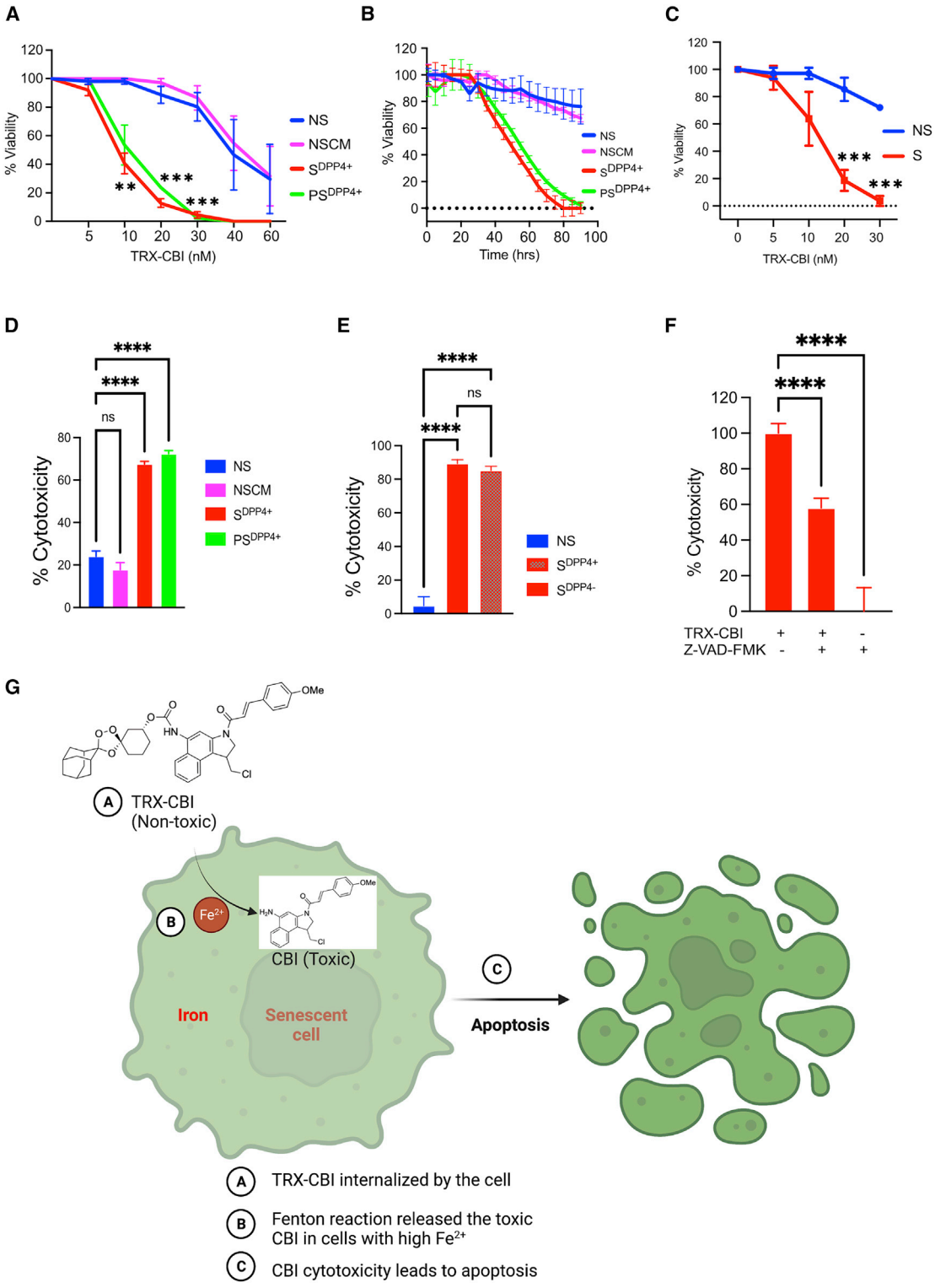


**Figure 7. Ferrous iron-activatable prodrug as a senolytic approach**

(A) Cytotoxicity of TRX-CBI in $S^{DPP4+}$ and $PS^{DPP4+}$ ECs.

(B) Cytotoxicity of 20 nM of TRX-CBI across time. Cells were treated with 20 nM of TRX-CBI, and viability was determined every 15 min for 4 days.

(C) Cytotoxicity of TRX-CBI in doxorubicin-treated senescent ECs without DPP4-based isolation.

(D) Cytotoxicity of TRX-CBI in etoposide-treated $S^{DPP4+}$ and $PS^{DPP4+}$ ECs.

*(legend continued on next page)*

Fer-1 further confirms the induction of ferroptosis as its senolysis mechanism (Figure 6).

Recently, another ferroptosis inducer, JQ1, which may downregulate both *SLC7A11* and *GPX4*, has also been shown to kill senescent human dermal fibroblasts.[56]

While this study was under review, another study showed that RSL3 selectively killed senescent tubular cells.[57] Several strategies to induce ferroptosis are being pursued for cancer therapy that might be repurposed for senotherapeutic purposes. However, ferroptosis inducer drugs such as GPX4 inhibitors may have several undesirable toxicities, as GPX4 is required for the development of normal adult mouse brain and kidney.[58–60]

We therefore investigated an alternative ferroptosis-independent strategy to ablate SCs by leveraging the elevated Fe(II) levels. In this study, we test a known Fe(II)-activated prodrug (TRX-CBI) as a senolytic agent. TRX-CBI is converted to the cytotoxic CBI in a manner dependent on the Fenton reaction promoted by Fe(II). Since SCs display elevated levels of Fe(II), TRX-CBI selectively ablates SCs independent of senescence lineage and cell type of origin. While the potent cytotoxicity of its CBI payload may limit the therapeutic index of TRX-CBI as a general senolytic, the TRX prodrug approach is generalizable to diverse classes of agents and might be employed to enhance specificity of current senolytics.

Our data show that prodrugs exploiting SCs' high Fe(II) pool such as TRX-CBI could be a safe and effective senolytic approach. Consistent with this, previous *in vivo* testing with TRX-CBI shows modest uptake in most tissues, with the pericardium, lungs, and liver exhibiting the highest uptake.[61] That study also showed that normal white matter had only half the Fe(II) burden of orthotopic glioma xenografts, and similarly that the level of Fe(II) in U87 MG xenografts as measured by PET was substantially higher than that of normal brain tissue.[61] Moreover, trioxolane-based compounds have been shown to have minimal penetrance across the blood-brain barrier,[62,63] likely shielding the brain from potential toxic effects. The potential value of a Fe(II)-based senolytic approach was further supported by our observation that the Fe(II) probe SiRhoNox-1 detects senescence independent of cell type of origin and mode of senescence induction with high selectivity.[50]

Recently, it was reported that iron, in its free form or when released from damaged red blood cells, is a potent trigger of cellular senescence *in vitro*. Iron accumulation is sufficient to initiate senescence, fibrogenesis, and inflammation.[64] In this context, when SCs are killed by senolytics, they can be expected to release high levels of iron, which might cause secondary senescence and initiate fibrosis. It has been reported that elimination of $p16^{High}$ liver sinusoid ECs induces liver and perivascular tissue fibrosis[29] and that treatment of a rat model of pulmonary hypertension with ABT263 improved pulmonary hypertension at 1 week but exacerbated it at 3 weeks, with loss of pulmonary ECs.[65] However, whether the release of iron from dead SCs contributes to this effect remains to be investigated. Finally, whether the release of iron to the circulation when SCs undergo apoptosis during senolytic treatment contributed to the unsuccessful clinical trials of several senolytic drugs remains to be investigated.

Our study focused on primary senescent human ECs, an understudied cell population in the senescence field of potentially great consequence. ECs line all blood vessels and function as a critical interface between the circulation and solid organs. They regulate many homeostatic functions like maintaining blood flow fluidity, clotting, and immune responses and inflammation, and they are most directly exposed both to the systemic signaling milieu, which has been found to play a critical role in aging (e.g., in the phenomena of heterochronic parabiosis[66] and therapeutic plasma exchange[67,68] as well as to the effects of circulating senescent immune cells).[69] Conversely, their free and extracellular vesicle-encapsulated SASP has the most direct access to the circulation, potentially giving senescent ECs the widest range of systemic effects of all SC types of origin. Senescent ECs have also been implicated in aging and several diseases of aging in mice[29,70–72] and human studies.[73,74]

Our data show that many of the most widely used senolytic drugs were especially toxic to human ECs. For instance, treatment with ABT-199, quercetin, and the combination of dasatinib and quercetin resulted in 50%, 75%, and 55% cytotoxicity in NSs at higher doses, respectively (Figure S3). It is possible that primary ECs are more sensitive to these drugs, which may explain the differences between (on the one hand) our results and those of Hwang et al.,[75] who also used primary adult human ECs, and (on the other hand) previously reported publications using HUVEC (e.g., Zhu et al.[76]) or non-ECs. Interestingly, there is only 30% loss in viability in NSs and NSCM ECs treated with FIN56 at high doses (Figure 5A) and a 40% loss in viability in IMR-90 fibroblasts (Figure 5B). Higher dose TRX-CBI also has up to 60% cytotoxicity toward NSs. Importantly, however, NSs and NSCM cells are far more tolerant to the optimal dose of TRX-CBI even for longer time exposure, with less than a 10% loss in viability in these cells treated with the drug vs. an over 90% loss in viability of S and PSs (Figure 7B). Notably the effects of FIN56 and TRX-CBI seem to be relatively safe to NS and NSCM controls from IMR-90 cells as well.

## Limitations of the study

Isolation of SCs using DPP4 enables us to dissect the differences and similarities between S and PSs. However, it should be noted that DPP4 is not a unique SC surface marker as several immune cells express DPP4 on their surface,[77,78] thus limiting the applicability of DPP4 as an SC surface marker for *in vivo* studies.

While our results show that a significant proportion of SCs express DPP4 on their surface, a substantial proportion of $DPP4^{-}$ cells also express multiple markers of senescence. This suggests the possibility of another distinct subset of $DPP4^{-}$ SCs

(E) Cytotoxicity of TRX-CBI in $S^{DPP4+}$ and $S^{DPP4-}$ ECs.
(F) Quantification of viable $S^{DPP4+}$ ECs (doxorubicin treated) 72 h after treatment with TRX-CBI alone or TRX-CBI + z-vad-fmk.
(G) Proposed mechanism of action of TRX-CBI cytotoxicity. See also Figures S5G–S5I. For (A)–(C), viability was determined by xCELLigence real-time cell analysis (RTCA) (n = 9 in three donors). Comparison was made with one-way ANOVA. Error bars represent mean ± SEM. $^{**}p < 0.01$, $^{***}p < 0.001$.

that remains to be further investigated. Further, as our RNA-seq comparison of S vs. PSs involves DPP4$^+$ cells, results of these experiments might not necessarily hold for DPP4$^-$ SCs, although we validated that our strategies informed by our RNA-seq also held in DPP4$^-$ cells, confirming the senolytic effects of FIN56 (Figures S6J and S6K) and TRX-CBI (Figure 7E) in these cells. Finally, it is possible that these results are limited to DPP4$^+$ SC, and validation of key findings in SCs isolated using another surface maker might be warranted.

We have demonstrated that targeting the aberrant iron metabolism of SCs, either with ferroptosis inducers or an Fe(II)-activated prodrug is a broad-spectrum senolytic approach. However, testing the current ferroptosis inducers as senolytic drugs *in vivo* will have limitations as they compromise the antioxidant system.[79,80] Fe(II)-activated prodrugs have previously been explored as a potential cancer therapy,[61] and our results provide the basis for investigating the potential of Fe(II)-activated prodrugs as senolytics to prevent and treat diseases of aging. However, further *in vivo* study is warranted to support the safety and efficacy of TRX-CBI or similar agents when used in the context of senolysis.

## STAR★METHODS

Detailed methods are provided in the online version of this paper and include the following:

- KEY RESOURCES TABLE
- RESOURCE AVAILABILITY
  - Lead contact
  - Materials availability
  - Data and code availability
- EXPERIMENTAL MODEL AND SUBJECT DETAILS
  - Cells
- METHOD DETAILS
  - Endothelial cells maintenance
  - Primary senescence induction
  - CM preparation and paracrine senescence induction
  - DPP4 flow cytometry
  - Isolation of senescent cells using DPP4 as a surface marker
  - Confirmation of senescence in DPP4+ isolated senescent cells
  - Senescence-associated beta-galactosidase
  - Immunofluorescence
  - Proliferation assay (Click-iT EdU staining)
  - RT-qPCR gene expression
  - Western blot
  - siRNA
  - Enzyme-linked immunosorbent assays (ELISA)
  - Senolytic drugs test
  - Total iron: Inductively coupled plasma optical-emission spectroscopy (ICP)
  - Ferrous iron measurement
  - Lipid peroxidation measurement
  - Real-time cytotoxicity assay (xCELLigence)
  - RNASeq
  - Pathway analysis
- QUANTIFICATION AND STATISTICAL ANALYSIS
  - Data representation and statistical analysis

## SUPPLEMENTAL INFORMATION

Supplemental information can be found online at https://doi.org/10.1016/j.celrep.2023.112058.

## ACKNOWLEDGMENTS

This work was supported by SENS Research Foundation (SRF) grant ID: SRF20190200P1. We would like to acknowledge Dr. David Killilea from University of California, San Francisco for total iron content analysis.

## AUTHOR CONTRIBUTIONS

T.D.A. and A. Sharma designed the study and wrote the manuscript. T.D.A. performed most experiments and analyzed results. T.D.A., R.A., and J.P.M. contributed to bioinformatics analysis. K.K was involved in western blot analysis and edited the manuscript. A.R., A. Stolzing, and M.R. participated in manuscript writing. R.L.G. and A.R.R. provided the TRX-CBI prodrug and participated in editing the manuscript.

## DECLARATION OF INTERESTS

J.P.M. is an advisor/consultant for the Longevity Vision Fund, NOVOS, Youth Bio Therapeutics, and the founder of Magellan Science Ltd, a company providing consulting services in longevity science. A.R.R. is a co-founder of Tatara Therapeutics Inc., which is developing iron-activated therapeutics.

Received: June 1, 2022
Revised: November 29, 2022
Accepted: January 17, 2023
Published: February 6, 2023

## REFERENCES

1. Lauren Medina, S.S., and Vespa, J. (2020). Living Longer: Historical and Projected Life Expectancy in the United States, 1960 to 2060 (Report February).
2. Rae, M.J., Butler, R.N., Campisi, J., de Grey, A.D.N.J., Finch, C.E., Gough, M., Martin, G.M., Vijg, J., Perrott, K.M., and Logan, B.J. (2010). The demographic and biomedical case for late-life interventions in aging. Sci. Transl. Med. *2*, 40cm21. https://doi.org/10.1126/scitranslmed.3000822.
3. Franceschi, C., Garagnani, P., Morsiani, C., Conte, M., Santoro, A., Grignolio, A., Monti, D., Capri, M., and Salvioli, S. (2018). The continuum of aging and age-related diseases: common mechanisms but different rates. Front. Med. *5*, 61. https://doi.org/10.3389/fmed.2018.00061.
4. Calimport, S.R.G., Bentley, B.L., Stewart, C.E., Pawelec, G., Scuteri, A., Vinciguerra, M., Slack, C., Chen, D., Harries, L.W., Marchant, G., et al. (2019). To help aging populations, classify organismal senescence. Science *366*, 576–578. https://doi.org/10.1126/science.aay7319.
5. Barzilai, N., Cuervo, A.M., and Austad, S. (2018). Aging as a biological target for prevention and therapy. JAMA *320*, 1321–1322. https://doi.org/10.1001/jama.2018.9562.
6. Hayflick, L., and Moorhead, P.S. (1961). The serial cultivation of human diploid cell strains. Exp. Cell Res. *25*, 585–621. https://doi.org/10.1016/0014-4827(61)90192-6.
7. Baker, D.J., Childs, B.G., Durik, M., Wijers, M.E., Sieben, C.J., Zhong, J., Saltness, R.A., Jeganathan, K.B., Verzosa, G.C., Pezeshki, A., et al. (2016). Naturally occurring p16(Ink4a)-positive cells shorten healthy lifespan. Nature *530*, 184–189. https://doi.org/10.1038/nature16932.
8. Baker, D.J., Wijshake, T., Tchkonia, T., LeBrasseur, N.K., Childs, B.G., van de Sluis, B., Kirkland, J.L., and van Deursen, J.M. (2011). Clearance of

p16Ink4a-positive senescent cells delays ageing-associated disorders. Nature *479*, 232–236. https://doi.org/10.1038/nature10600.

9. Childs, B.G., Gluscevic, M., Baker, D.J., Laberge, R.M., Marquess, D., Dananberg, J., and van Deursen, J.M. (2017). Senescent cells: an emerging target for diseases of ageing. Nat. Rev. Drug Discov. *16*, 718–735. https://doi.org/10.1038/nrd.2017.116.
10. Coppé, J.P., Desprez, P.Y., Krtolica, A., and Campisi, J. (2010). The senescence-associated secretory phenotype: the dark side of tumor suppression. Annu. Rev. Pathol. *5*, 99–118. https://doi.org/10.1146/annurev-pathol-121808-102144.
11. Olivieri, F., Prattichizzo, F., Grillari, J., and Balistreri, C.R. (2018). Cellular senescence and inflammaging in age-related diseases. Mediat. Inflamm. *2018*, 9076485. https://doi.org/10.1155/2018/9076485.
12. Birch, J., and Gil, J. (2020). Senescence and the SASP: many therapeutic avenues. Genes Dev. *34*, 1565–1576. https://doi.org/10.1101/gad.343129.120.
13. Xu, M., Pirtskhalava, T., Farr, J.N., Weigand, B.M., Palmer, A.K., Weivoda, M.M., Inman, C.L., Ogrodnik, M.B., Hachfeld, C.M., Fraser, D.G., et al. (2018). Senolytics improve physical function and increase lifespan in old age. Nat. Med. *24*, 1246–1256. https://doi.org/10.1038/s41591-018-0092-9.
14. Paez-Ribes, M., González-Gualda, E., Doherty, G.J., and Muñoz-Espín, D. (2019). Targeting senescent cells in translational medicine. EMBO Mol. Med. *11*, e10234. https://doi.org/10.15252/emmm.201810234.
15. Robbins, P.D., Jurk, D., Khosla, S., Kirkland, J.L., LeBrasseur, N.K., Miller, J.D., Passos, J.F., Pignolo, R.J., Tchkonia, T., and Niedernhofer, L.J. (2021). Senolytic drugs: reducing senescent cell viability to extend health span. Annu. Rev. Pharmacol. Toxicol. *61*, 779–803. https://doi.org/10.1146/annurev-pharmtox-050120-105018.
16. Casella, G., Munk, R., Kim, K.M., Piao, Y., De, S., Abdelmohsen, K., and Gorospe, M. (2019). Transcriptome signature of cellular senescence. Nucleic Acids Res. *47*, 7294–7305. https://doi.org/10.1093/nar/gkz555.
17. Hernandez-Segura, A., de Jong, T.V., Melov, S., Guryev, V., Campisi, J., and Demaria, M. (2017). Unmasking transcriptional heterogeneity in senescent cells. Curr. Biol. *27*, 2652–2660.e4. https://doi.org/10.1016/j.cub.2017.07.033.
18. Gasek, N.S., Kuchel, G.A., Kirkland, J.L., and Xu, M. (2021). Strategies for targeting senescent cells in human disease. Nat. Aging *1*, 870–879. https://doi.org/10.1038/s43587-021-00121-8.
19. Admasu, T.D., Rae, M., and Stolzing, A. (2021). Dissecting primary and secondary senescence to enable new senotherapeutic strategies. Ageing Res. Rev. *70*, 101412. https://doi.org/10.1016/j.arr.2021.101412.
20. Teo, Y.V., Rattanavirotkul, N., Olova, N., Salzano, A., Quintanilla, A., Tarrats, N., Kiourtis, C., Müller, M., Green, A.R., Adams, P.D., et al. (2019). Notch signaling mediates secondary senescence. Cell Rep. *27*, 997–1007.e5. https://doi.org/10.1016/j.celrep.2019.03.104.
21. Acosta, J.C., Banito, A., Wuestefeld, T., Georgilis, A., Janich, P., Morton, J.P., Athineos, D., Kang, T.W., Lasitschka, F., Andrulis, M., et al. (2013). A complex secretory program orchestrated by the inflammasome controls paracrine senescence. Nat. Cell Biol. *15*, 978–990. https://doi.org/10.1038/ncb2784.
22. Chen, H., Ruiz, P.D., McKimpson, W.M., Novikov, L., Kitsis, R.N., and Gamble, M.J. (2015). MacroH2A1 and ATM play opposing roles in paracrine senescence and the senescence-associated secretory phenotype. Mol. Cell *59*, 719–731. https://doi.org/10.1016/j.molcel.2015.07.011.
23. Borghesan, M., Fafián-Labora, J., Eleftheriadou, O., Carpintero-Fernández, P., Paez-Ribes, M., Vizcay-Barrena, G., Swisa, A., Kolodkin-Gal, D., Ximénez-Embún, P., Lowe, R., et al. (2019). Small extracellular vesicles are key regulators of non-cell autonomous intercellular communication in senescence via the interferon protein IFITM3. Cell Rep. *27*, 3956–3971.e6. https://doi.org/10.1016/j.celrep.2019.05.095.
24. Ferreira-Gonzalez, S., Lu, W.Y., Raven, A., Dwyer, B., Man, T.Y., O'Duibhir, E., Lewis, P.J.S., Campana, L., Kendall, T.J., Bird, T.G., et al. (2018). Paracrine cellular senescence exacerbates biliary injury and impairs regeneration. Nat. Commun. *9*, 1020. https://doi.org/10.1038/s41467-018-03299-5.
25. Kiourtis, C., Terradas-Terradas, M., Gee, L., Hsieh, Y.-C., Nixon, C., Clark, W., Shaw, R., Hanson, P., Sumpton, D., Mackay, G., et al. (2021). Inter-organ transmission of hepatocellular senescence induces multi-organ dysfunction through the TGFβ signalling pathway. Preprint at Research Square. https://doi.org/10.21203/rs.3.rs-1133747/v1.
26. Kim, K.M., Noh, J.H., Bodogai, M., Martindale, J.L., Yang, X., Indig, F.E., Basu, S.K., Ohnuma, K., Morimoto, C., Johnson, P.F., et al. (2017). Identification of senescent cell surface targetable protein DPP4. Genes Dev. *31*, 1529–1534. https://doi.org/10.1101/gad.302570.117.
27. Spangler, B., Fontaine, S.D., Shi, Y., Sambucetti, L., Mattis, A.N., Hann, B., Wells, J.A., and Renslo, A.R. (2016). A novel tumor-activated prodrug strategy targeting ferrous iron is effective in multiple preclinical cancer models. J. Med. Chem. *59*, 11161–11170. https://doi.org/10.1021/acs.jmedchem.6b01470.
28. Blank, B.R., Gonciarz, R.L., Talukder, P., Gut, J., Legac, J., Rosenthal, P.J., and Renslo, A.R. (2020). Antimalarial trioxolanes with superior drug-like properties and in vivo efficacy. ACS Infect. Dis. *6*, 1827–1835. https://doi.org/10.1021/acsinfecdis.0c00064.
29. Grosse, L., Wagner, N., Emelyanov, A., Molina, C., Lacas-Gervais, S., Wagner, K.D., and Bulavin, D.V. (2020). Defined p16(high) senescent cell types are indispensable for mouse healthspan. Cell Metabol. *32*, 87–99.e6. https://doi.org/10.1016/j.cmet.2020.05.002.
30. Hoare, M., Ito, Y., Kang, T.W., Weekes, M.P., Matheson, N.J., Patten, D.A., Shetty, S., Parry, A.J., Menon, S., Salama, R., et al. (2016). NOTCH1 mediates a switch between two distinct secretomes during senescence. Nat. Cell Biol. *18*, 979–992. https://doi.org/10.1038/ncb3397.
31. Zhu, Y., Tchkonia, T., Pirtskhalava, T., Gower, A.C., Ding, H., Giorgadze, N., Palmer, A.K., Ikeno, Y., Hubbard, G.B., Lenburg, M., et al. (2015). The Achilles' heel of senescent cells: from transcriptome to senolytic drugs. Aging Cell *14*, 644–658. https://doi.org/10.1111/acel.12344.
32. Mi, H., Ebert, D., Muruganujan, A., Mills, C., Albou, L.P., Mushayamaha, T., and Thomas, P.D. (2021). PANTHER version 16: a revised family classification, tree-based classification tool, enhancer regions and extensive API. Nucleic Acids Res. *49*, 394–403. https://doi.org/10.1093/nar/gkaa1106.
33. Liao, Y., Wang, J., Jaehnig, E.J., Shi, Z., and Zhang, B. (2019). WebGestalt 2019: gene set analysis toolkit with revamped UIs and APIs. Nucleic Acids Res. *47*, 199–205. https://doi.org/10.1093/nar/gkz401.
34. Basisty, N., Kale, A., Jeon, O.H., Kuehnemann, C., Payne, T., Rao, C., Holtz, A., Shah, S., Sharma, V., Ferrucci, L., et al. (2020). A proteomic atlas of senescence-associated secretomes for aging biomarker development. PLoS Biol. *18*, e3000599. https://doi.org/10.1371/journal.pbio.3000599.
35. Wiley, C.D., Liu, S., Limbad, C., Zawadzka, A.M., Beck, J., Demaria, M., Artwood, R., Alimirah, F., Lopez-Dominguez, J.A., Kuehnemann, C., et al. (2019). SILAC analysis reveals increased secretion of hemostasis-related factors by senescent cells. Cell Rep. *28*, 3329–3337.e5. https://doi.org/10.1016/j.celrep.2019.08.049.
36. Latini, F.R.M., Hemerly, J.P., Oler, G., Riggins, G.J., and Cerutti, J.M. (2008). Re-expression of ABI3-binding protein suppresses thyroid tumor growth by promoting senescence and inhibiting invasion. Endocr. Relat. Cancer *15*, 787–799. https://doi.org/10.1677/erc-08-0079.
37. Lin, L., Yee, S.W., Kim, R.B., and Giacomini, K.M. (2015). SLC transporters as therapeutic targets: emerging opportunities. Nat. Rev. Drug Discov. *14*, 543–560. https://doi.org/10.1038/nrd4626.
38. Coyle, P., Philcox, J.C., Carey, L.C., and Rofe, A.M. (2002). Metallothionein: the multipurpose protein. Cell. Mol. Life Sci. *59*, 627–647. https://doi.org/10.1007/s00018-002-8454-2.
39. Shimada, K., Skouta, R., Kaplan, A., Yang, W.S., Hayano, M., Dixon, S.J., Brown, L.M., Valenzuela, C.A., Wolpaw, A.J., and Stockwell, B.R. (2016). Global survey of cell death mechanisms reveals metabolic regulation

of ferroptosis. Nat. Chem. Biol. *12*, 497–503. https://doi.org/10.1038/nchembio.2079.

40. Yuan, H., Li, X., Zhang, X., Kang, R., and Tang, D. (2016). Identification of ACSL4 as a biomarker and contributor of ferroptosis. Biochem. Biophys. Res. Commun. *478*, 1338–1343. https://doi.org/10.1016/j.bbrc.2016.08.124.
41. Doll, S., Proneth, B., Tyurina, Y.Y., Panzilius, E., Kobayashi, S., Ingold, I., Irmler, M., Beckers, J., Aichler, M., Walch, A., et al. (2017). ACSL4 dictates ferroptosis sensitivity by shaping cellular lipid composition. Nat. Chem. Biol. *13*, 91–98. https://doi.org/10.1038/nchembio.2239.
42. Sun, Y., Coppé, J.P., and Lam, E.W.F. (2018). Cellular senescence: the sought or the unwanted? Trends Mol. Med. *24*, 871–885. https://doi.org/10.1016/j.molmed.2018.08.002.
43. Pignolo, R.J., Passos, J.F., Khosla, S., Tchkonia, T., and Kirkland, J.L. (2020). Reducing senescent cell burden in aging and disease. Trends Mol. Med. *26*, 630–638. https://doi.org/10.1016/j.molmed.2020.03.005.
44. Kirkland, J.L., and Tchkonia, T. (2020). Senolytic drugs: from discovery to translation. J. Intern. Med. *288*, 518–536. https://doi.org/10.1111/joim.13141.
45. Malaquin, N., Vancayseele, A., Gilbert, S., Antenor-Habazac, L., Olivier, M.A., Ait Ali Brahem, Z., Saad, F., Delouya, G., and Rodier, F. (2020). DNA damage- but not enzalutamide-induced senescence in prostate cancer promotes senolytic bcl-xL inhibitor sensitivity. Cells *9*. https://doi.org/10.3390/cells9071593.
46. Yosef, R., Pilpel, N., Tokarsky-Amiel, R., Biran, A., Ovadya, Y., Cohen, S., Vadai, E., Dassa, L., Shahar, E., Condiotti, R., et al. (2016). Directed elimination of senescent cells by inhibition of BCL-W and BCL-XL. Nat. Commun. *7*, 11190. https://doi.org/10.1038/ncomms11190.
47. Masaldan, S., Clatworthy, S.A.S., Gamell, C., Meggyesy, P.M., Rigopoulos, A.T., Haupt, S., Haupt, Y., Denoyer, D., Adlard, P.A., Bush, A.I., and Cater, M.A. (2018). Iron accumulation in senescent cells is coupled with impaired ferritinophagy and inhibition of ferroptosis. Redox Biol. *14*, 100–115. https://doi.org/10.1016/j.redox.2017.08.015.
48. Venkatesh, D., Stockwell, B.R., and Prives, C. (2020). p21 can be a barrier to ferroptosis independent of p53. Aging (Albany NY) *12*, 17800–17814. https://doi.org/10.18632/aging.103961.
49. Dixon, S.J., and Stockwell, B.R. (2019). The hallmarks of ferroptosis. Annu. Rev. Cell Biol. *3*, 35–54. https://doi.org/10.1146/annurev-cancerbio-030518-055844.
50. Parella, K.J., Manhardt, C., Capucilli, D., Moyer, B., Colegrove, H., Moody, K.J., Sleeper, M., Banas, A., Rebbaa, A., and Wolfe, A.J. (2021). Fluorescence-based detection of ferrous iron in senescent cells. Rejuvenation Res. *24*, 456–463. https://doi.org/10.1089/rej.2021.0075.
51. MacKenzie, E.L., Iwasaki, K., and Tsuji, Y. (2008). Intracellular iron transport and storage: from molecular mechanisms to health implications. Antioxidants Redox Signal. *10*, 997–1030. https://doi.org/10.1089/ars.2007.1893.
52. Wallace, D.F. (2016). The regulation of iron absorption and homeostasis. Clin. Biochem. Rev. *37*, 51–62.
53. Chen, X., Comish, P.B., Tang, D., and Kang, R. (2021). Characteristics and biomarkers of ferroptosis. Front. Cell Dev. Biol. *9*, 637162. https://doi.org/10.3389/fcell.2021.637162.
54. Tang, D., Chen, X., Kang, R., and Kroemer, G. (2021). Ferroptosis: molecular mechanisms and health implications. Cell Res. *31*, 107–125. https://doi.org/10.1038/s41422-020-00441-1.
55. Zhang, X., Guo, Y., Li, H., and Han, L. (2021). FIN56, a novel ferroptosis inducer, triggers lysosomal membrane permeabilization in a TFEB-dependent manner in glioblastoma. J. Cancer *12*, 6610–6619. https://doi.org/10.7150/jca.58500.
56. Go, S., Kang, M., Kwon, S.P., Jung, M., Jeon, O.H., and Kim, B.S. (2021). The senolytic drug JQ1 removes senescent cells via ferroptosis. Tissue Eng. Regen. Med. *18*, 841–850. https://doi.org/10.1007/s13770-021-00346-z.
57. Liao, C.M., Wulfmeyer, V.C., Chen, R., Erlangga, Z., Sinning, J., von Mässenhausen, A., Sörensen-Zender, I., Beer, K., von Vietinghoff, S., Haller, H., et al. (2022). Induction of ferroptosis selectively eliminates senescent tubular cells. Am. J. Transplant. *22*, 2158–2168. https://doi.org/10.1111/ajt.17102.
58. Friedmann Angeli, J.P., Schneider, M., Proneth, B., Tyurina, Y.Y., Tyurin, V.A., Hammond, V.J., Herbach, N., Aichler, M., Walch, A., Eggenhofer, E., et al. (2014). Inactivation of the ferroptosis regulator Gpx4 triggers acute renal failure in mice. Nat. Cell Biol. *16*, 1180–1191. https://doi.org/10.1038/ncb3064.
59. Yoo, S.E., Chen, L., Na, R., Liu, Y., Rios, C., Van Remmen, H., Richardson, A., and Ran, Q. (2012). Gpx4 ablation in adult mice results in a lethal phenotype accompanied by neuronal loss in brain. Free Radic. Biol. Med. *52*, 1820–1827. https://doi.org/10.1016/j.freeradbiomed.2012.02.043.
60. Hambright, W.S., Fonseca, R.S., Chen, L., Na, R., and Ran, Q. (2017). Ablation of ferroptosis regulator glutathione peroxidase 4 in forebrain neurons promotes cognitive impairment and neurodegeneration. Redox Biol. *12*, 8–17. https://doi.org/10.1016/j.redox.2017.01.021.
61. Zhao, N., Huang, Y., Wang, Y.H., Muir, R.K., Chen, Y.C., Wei, J., Hooshdaran, N., Viswanath, P., Seo, Y., Ruggero, D., et al. (2021). Ferronostics: measuring tumoral ferrous iron with PET to predict sensitivity to iron-targeted cancer therapies. J. Nucl. Med. *62*, 949–955. https://doi.org/10.2967/jnumed.120.252460.
62. Muir, R.K., Zhao, N., Wei, J., Wang, Y.H., Moroz, A., Huang, Y., Chen, Y.C., Sriram, R., Kurhanewicz, J., Ruggero, D., et al. (2019). Measuring dynamic changes in the labile iron pool in vivo with a reactivity-based probe for positron emission tomography. ACS Cent. Sci. *5*, 727–736. https://doi.org/10.1021/acscentsci.9b00240.
63. Lauterwasser, E.M.W., Fontaine, S.D., Li, H., Gut, J., Katneni, K., Charman, S.A., Rosenthal, P.J., Bogyo, M., and Renslo, A.R. (2015). Trioxolane-mediated delivery of mefloquine limits brain exposure in a mouse model of malaria. ACS Med. Chem. Lett. *6*, 1145–1149. https://doi.org/10.1021/acsmedchemlett.5b00296.
64. Maus, M., López-Polo, V., Lafarga, M., Aguilera, M., Lama, E.D., Meyer, K., Manonelles, A., Sola, A., Martinez, C.L., López-Alonso, I., et al. (2022). Iron accumulation drives fibrosis, senescence, and the senescence-associated secretory phenotype. Preprint at bioRxiv. https://doi.org/10.1101/2022.07.29.501953.
65. Born, E., Lipskaia, L., Breau, M., Houssaini, A., Beaulieu, D.P., Marcos, E., Pierre, R., Do Cruzeiro, M., Lefevre, M., Derumeaux, G., et al. (2022). Eliminating senescent cells can promote pulmonary hypertension development and progression. Preprint at Circulation. https://doi.org/10.1161/circulationaha.122.058794.
66. Conboy, M.J., Conboy, I.M., and Rando, T.A. (2013). Heterochronic parabiosis: historical perspective and methodological considerations for studies of aging and longevity. Aging Cell *12*, 525–530. https://doi.org/10.1111/acel.12065.
67. Mehdipour, M., Skinner, C., Wong, N., Lieb, M., Liu, C., Etienne, J., Kato, C., Kiprov, D., Conboy, M.J., and Conboy, I.M. (2020). Rejuvenation of three germ layers tissues by exchanging old blood plasma with saline-albumin. Aging (Albany NY) *12*, 8790–8819. https://doi.org/10.18632/aging.103418.
68. Mehdipour, M., Mehdipour, T., Skinner, C.M., Wong, N., Liu, C., Chen, C.C., Jeon, O.H., Zuo, Y., Conboy, M.J., and Conboy, I.M. (2021). Plasma dilution improves cognition and attenuates neuroinflammation in old mice. Geroscience *43*, 1–18. https://doi.org/10.1007/s11357-020-00297-8.
69. Yousefzadeh, M.J., Flores, R.R., Zhu, Y., Schmiechen, Z.C., Brooks, R.W., Trussoni, C.E., Cui, Y., Angelini, L., Lee, K.A., McGowan, S.J., et al. (2021). An aged immune system drives senescence and ageing of solid organs. Nature *594*, 100–105. https://doi.org/10.1038/s41586-021-03547-7.
70. Yousefzadeh, M.J., Zhao, J., Bukata, C., Wade, E.A., McGowan, S.J., Angelini, L.A., Bank, M.P., Gurkar, A.U., McGuckian, C.A., Calubag, M.F., et al. (2020). Tissue specificity of senescent cell accumulation during

physiologic and accelerated aging of mice. Aging Cell *19*, e13094. https://doi.org/10.1111/acel.13094.

71. Kiss, T., Nyúl-Tóth, Á., Balasubramanian, P., Tarantini, S., Ahire, C., DelFavero, J., Yabluchanskiy, A., Csipo, T., Farkas, E., Wiley, G., et al. (2020). Single-cell RNA sequencing identifies senescent cerebromicrovascular endothelial cells in the aged mouse brain. Geroscience *42*, 429–444. https://doi.org/10.1007/s11357-020-00177-1.
72. Ting, K.K., Coleman, P., Zhao, Y., Vadas, M.A., and Gamble, J.R. (2021). The aging endothelium. Vasc. Biol. *3*, 35–47. https://doi.org/10.1530/vb-20-0013.
73. Rossman, M.J., Kaplon, R.E., Hill, S.D., McNamara, M.N., Santos-Parker, J.R., Pierce, G.L., Seals, D.R., and Donato, A.J. (2017). Endothelial cell senescence with aging in healthy humans: prevention by habitual exercise and relation to vascular endothelial function. Am. J. Physiol. Heart Circ. Physiol. *313*, 890–895. https://doi.org/10.1152/ajpheart.00416.2017.
74. Villaret, A., Galitzky, J., Decaunes, P., Estève, D., Marques, M.A., Sengenès, C., Chiotasso, P., Tchkonia, T., Lafontan, M., Kirkland, J.L., and Bouloumié, A. (2010). Adipose tissue endothelial cells from obese human subjects: differences among depots in angiogenic, metabolic, and inflammatory gene expression and cellular senescence. Diabetes *59*, 2755–2763. https://doi.org/10.2337/db10-0398.
75. Hwang, H.V., Tran, D.T., Rebuffatti, M.N., Li, C.S., and Knowlton, A.A. (2018). Investigation of quercetin and hyperoside as senolytics in adult human endothelial cells. PLoS One *13*, e0190374. https://doi.org/10.1371/journal.pone.0190374.
76. Zhu, Y., Tchkonia, T., Fuhrmann-Stroissnigg, H., Dai, H.M., Ling, Y.Y., Stout, M.B., Pirtskhalava, T., Giorgadze, N., Johnson, K.O., Giles, C.B., et al. (2016). Identification of a novel senolytic agent, navitoclax, targeting the Bcl-2 family of anti-apoptotic factors. Aging Cell *15*, 428–435. https://doi.org/10.1111/acel.12445.
77. Kameoka, J., Tanaka, T., Nojima, Y., Schlossman, S.F., and Morimoto, C. (1993). Direct association of adenosine deaminase with a T cell activation antigen, CD26. Science *261*, 466–469. https://doi.org/10.1126/science.8101391.
78. Ohnuma, K., Dang, N.H., and Morimoto, C. (2008). Revisiting an old acquaintance: CD26 and its molecular mechanisms in T cell function. Trends Immunol. *29*, 295–301. https://doi.org/10.1016/j.it.2008.02.010.
79. Kuang, F., Liu, J., Tang, D., and Kang, R. (2020). Oxidative damage and antioxidant defense in ferroptosis. Front. Cell Dev. Biol. *8*, 586578. https://doi.org/10.3389/fcell.2020.586578.
80. Liu, M., Kong, X.-Y., Yao, Y., Wang, X.-A., Yang, W., Wu, H., Li, S., Ding, J.-W., and Yang, J. (2022). The critical role and molecular mechanisms of ferroptosis in antioxidant systems: a narrative review. Ann. Transl. Med. *10*, 368.
81. Dimri, G.P., Lee, X., Basile, G., Acosta, M., Scott, G., Roskelley, C., Medrano, E.E., Linskens, M., Rubelj, I., Pereira-Smith, O., et al. (1995). A biomarker that identifies senescent human cells in culture and in aging skin in vivo. Proc. Natl. Acad. Sci. USA *92*, 9363–9367. https://doi.org/10.1073/pnas.92.20.9363.
82. Killilea, D.W., Atamna, H., Liao, C., and Ames, B.N. (2003). Iron accumulation during cellular senescence in human fibroblasts in vitro. Antioxidants Redox Signal. *5*, 507–516. https://doi.org/10.1089/152308603770310158.
83. Love, M.I., Huber, W., and Anders, S. (2014). Moderated estimation of fold change and dispersion for RNA-seq data with DESeq2. Genome Biol. *15*, 550. https://doi.org/10.1186/s13059-014-0550-8.
84. Bourgon, R., Gentleman, R., and Huber, W. (2010). Independent filtering increases detection power for high-throughput experiments. Proc. Natl. Acad. Sci. USA *107*, 9546–9551. https://doi.org/10.1073/pnas.0914005107.
85. Cook, R.D. (1977). Detection of influential observation in linear regression. Technometrics *19*, 15–18.
86. Blighe, K., Rana, S., and Lewis, M. (2020). EnhancedVolcano: Publication-Ready Volcano Plots with Enhanced Colouring and Labeling.
87. Kolde, R. (2019). Pheatmap: Pretty Heatmaps.

## STAR★METHODS

### KEY RESOURCES TABLE

| REAGENT or RESOURCE | SOURCE | IDENTIFIER |
|---|---|---|
| Antibodies | | |
| Anti-γH2ax (P Ser139) antibody | Novus | NB100-74435 |
| Anti-HMGB1 antibody | Abcam | ab18256 |
| Anti-DPP4 (D6D8K) antibody | Cell Signaling technology | 67138 |
| Anti-Bcl-2 antibody | Cell Signaling technology | D55G8 |
| Anti-Bcl-xl antibody | Cell Signaling technology | 2762 |
| Anti-Bcl-w antibody | Cell Signaling technology | 2724 |
| Anti-ActB antibody | Cell Signaling technology | 4967 |
| Anti-CD26 antibody | BD Bioscience | 555437 |
| Anti-Rabbit IgG H&L (HRP) | Abcam | ab6802 |
| Anti-TFRC antibody | Santa Cruz biotechnology | sc-65882 |
| Anti-p16 antibody | Santa Cruz biotechnology | JC8 |
| Anti-ferroportin antibody | Santa Cruz biotechnology | sc-518125 |
| Anti-FTH1 antibody | Cell Signaling technology | 3998 |
| Anti-ACSL4 antibody | ABclonal | A16848 |
| Anti-GPx4 antibody | Cell Signaling technology | 52455 |
| Chemicals, peptides, and recombinant proteins | | |
| ABT-199 | Selleckchem | S8048 |
| ABT-263 | Selleckchem | S1001 |
| Quercetin | Sigma Aldrich | PHR1488 |
| Dasatinib | LC Laboratories | D-3307 |
| FIN56 | Selleckchem | HY-103087 |
| Fer-1 | Selleckchem | S7243 |
| z-VAD-FMK | Selleckchem | S7023 |
| Deferiprone | Selleckchem | S4067 |
| Doxorubicin | Millipore Sigma | 5,040,420,001 |
| FeroFarRed | Merck | SCT037 |
| Crystal Violet | Millipore Sigma | C0775 |
| Critical commercial assays | | |
| Senescence Detection Kit | BioVision | K320 |
| IL-6 ELISA kit | ThermoFisher | KHC0061 |
| IL-8 ELISA kit | ThermoFisher | BMS204-3 |
| TBARS Assay Kit | Cayman chemical | 10,009,055 |
| LIVE/DEAD™ Viability/Cytotoxicity Kit | Invitrogen | L3224 |
| Quick-RNA Miniprep Kit | Zymo Research | R1055 |
| Reverse Transcription System | Takara | RR036A |
| Hoechst | Invitrogen | H3570 |
| C11 Bodipy | Cayman chemical | 27,086 |
| Anti-PE MicroBeads UltraPure | Miltenyi biotec | 130-048-801 |
| Click-iT EdU | ThermoFisher | C10337 |
| ON-TARGETplus siGPx4 | Horizon Discovery | 011,676-00-0005 |
| ON-TARGETplus Non-targeting Pool | Horizon Discovery | D-001810-10–05 |
| Lipofectamine 3000 | ThermoFisher | L3000015 |

(*Continued on next page*)

*Continued*

| REAGENT or RESOURCE | SOURCE | IDENTIFIER |
|---|---|---|
| Deposited data | | |
| Raw and Processed RNA-Seq data | This paper | GEO: GSE196724 |
| Experimental models: Cell lines | | |
| IMR-90 | ATCC | CCL-186 |
| MSC | ATCC | SCRC-4000 |
| Endothelial cells | Coriell Institute | AG09872 |
| Endothelial cells | Coriell Institute | AG10774 |
| Endothelial cells | Coriell Institute | AG10770 |
| Oligonucleotides | | |
| P16 TaqMan probe | ThermoFisher | Hs00923894_m1 |
| P21 TaqMan probe | ThermoFisher | Hs01040810_m1 |
| IL-6 TaqMan probe | ThermoFisher | Hs00174131_m1 |
| IL-8 TaqMan probe | ThermoFisher | Hs00174103_m1 |
| LMNB1 TaqMan probe | ThermoFisher | Hs01059205_m1 |
| FTRC TaqMan probe | ThermoFisher | Hs00951086_m1 |
| GDF7 TaqMan probe | ThermoFisher | Hs00766203_m1 |
| WNT5B TaqMan probe | ThermoFisher | Hs01086864_m1 |
| IGFBP5 TaqMan probe | ThermoFisher | Hs00181213_m1 |
| CST1 TaqMan probe | ThermoFisher | Hs00606961_m1 |
| IGFBP3 TaqMan probe | ThermoFisher | Hs00181211_m1 |
| PAPPA2 TaqMan probe | ThermoFisher | Hs00535718_m1 |
| EPHA7 TaqMan probe | ThermoFisher | Hs01033006_m1 |
| TNC TaqMan probe | ThermoFisher | Hs01115665_m1 |
| MT1G TaqMan probe | ThermoFisher | Hs04401199_s1 |
| TGFB TaqMan probe | ThermoFisher | Hs00610319_m1 |
| ACSL4 TaqMan probe | ThermoFisher | Hs01547083_m1 |
| PTGS2 TaqMan probe | ThermoFisher | Hs01573477_g1 |
| CHAC1 TaqMan probe | ThermoFisher | Hs03043929_m1 |
| NFE2L2 TaqMan probe | ThermoFisher | Hs00975961_g1 |
| FDFT1 TaqMan probe | ThermoFisher | Hs00926054_m1 |
| GPx4 TaqMan probe | ThermoFisher | Hs00157812_m1 |
| SLC7A11 TaqMan probe | ThermoFisher | Hs00921938_m1 |
| Software and algorithms | | |
| ImageJ | NIH | https://imagej.nih.gov/ij/ |
| Flowlogic | Flowlogic™ | https://flowlogic.software/ |
| RTCA software | Agilent | 310,100,240 |
| GraphPad prism 9 | GraphPad software | https://www.graphpad.com/ |
| Endnote 20 | Endnote | https://endnote.com/ |
| R statistical package | R core team | https://www.r-project.org/ |

## RESOURCE AVAILABILITY

### Lead contact

Further information and requests for resources and reagents should be directed to and will be fulfilled by the lead contact, Tesfahun Admasu: dessaletesfahun@gmail.com.

### Materials availability

This study did not generate unique reagents.

### Data and code availability

All sequencing data that support the findings of this study have been deposited in the National Center for Biotechnology Information Gene Expression Omnibus (GEO). The accession number for the sequence reported in this paper is (GEO: GSE196724). The sequence data reported in this paper will be shared by the lead contact upon request. This paper does not report original code. Any additional information required to reanalyze the data reported in this paper is available from the lead contact upon request.

## EXPERIMENTAL MODEL AND SUBJECT DETAILS

### Cells

All endothelial cells were purchased from Coriell Institute for medical research and IMR-90 was purchased from the American Type Culture Collection (ATCC), see key resources table. Human primary endothelial cells were the primary cell type used in this study. IMR-90 and MSC cells were cultured in Dulbecco's modified eagle medium (DMEM 4.5 g/L glucose, without sodium pyruvate - Gibco) supplemented with 10% FBS and penicillin/streptomycin (Gibco). Quiescence was induced by replacing culture media with media containing 0.2% FBS for 24 h before analysis. All cells were cultured at 37°C and 5% $O_2$. All cells were mycoplasma free.

## METHOD DETAILS

### Endothelial cells maintenance

All cells were purchased from Coriell Institute for medical research. Primary human endothelial cells from three apparently healthy individuals (AG09872, AG10774, AG10770) were cultured using promo cell basal medium MV2 (C-22221) supplemented with Growth Medium MV 2 Supplement Pack (C-39221). All cells were cultured at 37°C and 20% $O_2$. All cells were mycoplasma free. Quiescence was induced by replacing culture media with low serum medium 24hrs before analysis.

### Primary senescence induction

Senescence was induced by treating cells with 250 μM doxorubicin for 24hrs. After 24hrs doxorubicin was removed and cells were maintained in complete medium for 9 days. At day 9 the complete medium was changed to low serum medium and after 24hrs multiple senescence markers were determined both on the cells and conditioned medium (CM) collected.

### CM preparation and paracrine senescence induction

Primary senescence has been induced as above and CM were generated by culturing cells in appropriate low serum media for 24hrs before harvest. CM collected was spun down to remove cell debris and the supernatant was used to induce paracrine senescence. Cells were then detrached with TrypLE Select Enzyme and counted using Invitrogen Countess 3 Automated Cell Counter. All quantitative assays for CM (e.g ELISA) were normalized to cell number. For paracrine senescence induction, sub-confluent cells were treated with 50% CM collected from primary senescent cells and 50% complete medium for 6 days. Sub confluent cells treated with CM collected from quiescent cells were used as a control. Media was changed every other day and at day 6 medium was replaced with low serum medium. At day 7 multiple senescence markers were determined.

### DPP4 flow cytometry

To determine the expression of DPP4 in senescent cells, primary and paracrine senescence has been induced in different cell cultures as described above. Cells were resuspended to a concentration of $1 \times 10^6$ cells/mL and aliquoted. Cells were fixed with ice-cold 100% methanol at −20°C for 20 min, wash two times with 1X PBS and resuspended in FACS buffer (1% BSA in PBS +0.01% sodium azide). Cells were then incubated with DPP4-PE conjugated antibody (PE Mouse anti-Human CD26 (BD Bioscience Cat 555437 lot 9,192,757, Clone M-A261 (RUO)) (20ul per million cells) for 1 h at room temperature in the dark. After 1hr incubation, cells were washed three times with FACS buffer and resuspend in 300μL FACS buffer. Finally, cells were pass through a mesh filter of 40 μm pore size to exclude any clumps of cells and expression of DPP4 were determined by flow cytometer (DB Accuri C6). DPP4 was stained as described below (immunofluorescence section) without permeabilization using DPP4/CD26 (D6D8K) Rabbit mAb #67138 (Cell Signaling technology). Unstained cells and cells stained with secondary antibody only were used as a negative control. PI staining were used to exclude dead cells. Data analysis was done using Flowlogic software. DPP4+ cells were gated based on the isotype control and percent of DPP4+ cells were calculated.

### Isolation of senescent cells using DPP4 as a surface marker

Primary and paracrine senescent cells were collected, and resuspended cell pellet were stained with PE-conjugated DPP4 antibody in the dark at 4°C for 30 min. Cells were washed twice with a MACS buffer (PBS, 0.5% BSA, and 2 mM EDTA) to remove unbound antibody. Cells were resuspended with 80uL MACS buffer per $10^7$ total cells and incubate with 20ul of Anti-PE MicroBeads UltraPure (miltenyi biotec 130-048-801, lot 5,200,405,519) at 4°C for 15 min. Cells were washed and resuspended with 500ul buffer. Cell

suspension was run over MS Column attached to MidiMACS Separator (miltenyi biotec) and unlabeled cells that pass through the column were collected (DPP4 negative cells). Then, the column was removed from the MidiMACS Separator and magnetically labeled bound cells were collected.

### Confirmation of senescence in DPP4+ isolated senescent cells

DPP4 positive cells isolated as above were re-plated with complete medium for 24hrs and multiple senescence markers were determined as described below.

### Senescence-associated beta-galactosidase

SA-β Gal activity was detected as described[81] using a commercial kit (Biovision).

### Immunofluorescence

10,000 cells per well were plated in 96 well plate and senescence induced as above. Cells were fixed with 4% PFA for 15 min at room temperature. After washing away the fixative solution with PBS, cells were permeabilized with 0.5% Triton for 15 min, blocked in 5% BSA in PBS for 30 min and incubated overnight with primary antibody at 4°C. Primary antibodies used were gamma $\gamma H_2AX$ (P Ser139) Mouse Antibody (3F2), NB100-74435 (Novus) (1:1000 dilution with 5% BSA in PBS) and Anti-HMGB1 antibody (ab18256), Rabbit, (Abcam) (1:500 dilution with 5% BSA in PBS). DPP4 immunofluorescence were performed without permeabilization using DPP4/CD26 (D6D8K) Rabbit mAb #67138 (Cell Signaling technology, 1:200 dilution with 5% BSA in PBS). Cells were then washed with PBS and incubated with fluorescent secondary antibody and Hoechst (Invitrogen H3570) (1: 1000 in 5% BSA in PBS) for 20 min at room temperature in dark. Secondary antibodies used were Invitrogen Goat anti-Rabbit IgG (H + L) Cross-Adsorbed Secondary Antibody, Alexa Fluor 488 (Catalog # A-11008, lot 1,166,843) and Invitrogen Goat anti-Mouse IgG (H + L) Highly Cross-Adsorbed Secondary Antibody, Alexa Fluor 546 (Catalog # A-11030). Images were acquired with Molecular Devices ImageExpress Macro. Images processing and image overlay was done with ImageJ software.

### Proliferation assay (Click-iT EdU staining)

Cell proliferation was determined by Click-iT EdU Cell Proliferation Kit (ThermoFisher, C10337) following the manufacturer protocol. Briefly, cells were cultured with EdU (10 μM) for 24hrs, fixed in 4% PFA for 10 min, washed in PBS, and permeabilized with 0.5% Triton X-100 for 15 min. Cells were then washed and incubated in Click-iT reaction cocktail and DNA was stained with Hoechst 33,342 (Invitrogen H3570). Images were acquired by ZEISS Axiovert S 100 microscope at a magnification of 32x. Number of proliferating cells were determined by counting number of cells positive for Click-iT EdU. Total number of cells were counted based on Hoechst 33,342 staining. Fraction proliferating cells were determined by dividing number of proliferating cells to the total number of cells.

### RT-qPCR gene expression

RNA was extracted using commercially available kits Quick-RNA Miniprep Kit (Zymo Research, R1055) according to the manufacturer's instructions. cDNA synthesis was performed using Takara PrimeScript RT Master Mix (Cat. # RR036A) according to the manufacturer's instructions. Quantitative PCR was performed on a StepOnePlus Real-Time PCR System (ThermoFisher) using primers and probes purchased from Applied Biosystems TaqMan Gene Expression assays. Primers and probes used are listed above (key resources table).

### Western blot

Cells were lysed in RIPA buffer (Cell Signaling technology, Catalog # 9806S), supplemented with protease-phosphatase inhibitor cocktail (Cell Signaling technology, Catalog # 5871). Cell suspensions were incubated for 10 min on ice, followed by microcentrifugation at 4°C for 15 min to clear the lysate of cell debris. Protein concentration was determined by BCA Protein Assay (Thermo Scientific, Catalog # 23227). 20μg of protein was separated by electrophoresis and transferred to PVDF membranes (Bio-Rad, Catalog # 1620177) using a semi-dry transfer apparatus (Bio-Rad). Membranes were incubated with primary antibody overnight at 4°C, followed by incubation with secondary antibody for 1 h at room temperature. Blots were developed using Pierce ECL Western Blotting substrate (Thermo Scientific; Cat# 32209) and visualized by GeneGnome chemiluminescence imaging system. All antibodies used in this study are listed in key resources table.

### siRNA

For GPX4 silencing experiments, senescent and non-senescent IMR90 fibroblasts were transfected with siCtrl or ON-TARGETplus siGPX4 SMARTpool (25 nM) (Dharmacon). Small RNA transfections were performed using Lipofectamine 3000 (Thermo Fisher Scientific).

### Enzyme-linked immunosorbent assays (ELISA)

Primary and paracrine senescence was induced as indicated above and cultured in low serum medium for 24hrs. CM was collected, and cell debris were removed by centrifugation at 300G for 10 min. Supernatants were transferred to a tube on ice; cells were trypsinized and counted by trypan Blue assay. IL-6 and IL-8 levels in the CM was analyzed by ELISA kits as instructed by the manufacturer and normalized to the cell number.

### Senolytic drugs test

Cells were cultured in T175 flasks and 7 days after senescence induction DPP4+ SCs were isolated and replated to 96 well plates. 24hrs after replating all suspended cells were removed and live attached cells were treated with senolytic drugs. ABT-199, ABT-263 and FIN56 were purchased from Selleckchem and dasatinib were from LC laboratories. Quercetin was purchased from Sigma-Aldrich. TRX-CBI was synthesized by Renslo group at University of California, San Francisco. 24hrs after the first treatment cells were received fresh TRX-CBI. Cell viability was determined using Real-time cytotoxicity assay (xCELLigence), LIVE/DEAD Viability/Cytotoxicity Kit (Invitrogen, L3224) or crystal violet assay following the manufacturer protocol (see below for details). Cytotoxicity was determined in three independent experiments in triplicates for each donor and cell types.

### Total iron: Inductively coupled plasma optical-emission spectroscopy (ICP)

Cells were harvested, counted in triplicate, and processed for iron analysis as described.[82]

### Ferrous iron measurement

Ferrous iron content of cells was determined by FerroFarRed also known as SiRhoNox-1 fluorescent probe based on manufacturers protocol. Briefly, culture medium was removed from flasks and 8 well chambers and cells rinsed three times with PBS buffer. Cells were then treated with 5 μM of FerroFarRed diluted with serum-free cell culture medium and incubated for 1 h at 37°C. After staining, excess probe was washed off with PBS and cells were collected for flow analysis or imaged in 8 well chambers. Flow analysis was done using Flowlogic software. SiRhoNox-1 positive cells were gated using unstained cells as a negative control and percent of SiRhoNox-1 positive cells were determined.

### Lipid peroxidation measurement

ECs were seeded in 6-well plates and 8 well chambers. Seven days after senescence induction cells in 6 well plates were harvested, and cell numbers were determined. MDA level was measured by a commercial TBARS Assay Kit according to the manufacturer's instructions. Oxidized lipid content of cells was determined using C11 Bodipy dye following the manufacturers protocol.

### Real-time cytotoxicity assay (xCELLigence)

A 50μL medium was added to E-Plates 96 (Agilent) for measurement of background values. DPP4+ isolated primary and paracrine SCs and their respective non senescent cells were seeded in an additional 100μL medium at a density of 10,000 cells per well. Cell attachment was monitored using the RTCA MP (Agilent) instrument and the RTCA software (Agilent) until the plateau phase was reached, which was usually after approximately 24hrs. Floating cells were removed, and drugs were added at a range of doses. Cells treated with 0.2% Triton x-100 was used as a 100% dead cell positive control for cytotoxicity assay. Upon addition of drugs, impedance measurements were performed every 15 min for up to three days. All experiments were performed at least in triplicates in three independent experiments for each donor and cell types. Changes in impedance were expressed as a cell index (CI) value, which derives from relative impedance changes corresponding to cellular coverage of the electrode sensors, normalized to baseline impedance values with medium only. Percent cytotoxicity was determined based on the relative CI value. To analyze the acquired data, CI values were exported, and percentage of lysis was calculated in relation to the control cells lacking any drug.

### RNASeq

RNASeq analysis were conducted in DPP4+ primary and paracrine senescent ECs from three donors each in triplicates. DPP4 positive SCs were collected as above and stored at −80°C in RNAZip. RNA was extracted using commercially available kits (Quick-RNA Miniprep Kit (Zymo Research, R1055) according to the manufacturer's instructions. cDNA synthesis was performed using Takara PrimeScript RT Master Mix (Cat. # RR036A) according to the manufacturer's instructions. Afterward, RNA was quantified photometrically with Nano Drop 2000 and stored at −80C until use. The integrity of total RNA was measured by Agilent Bioanalyzer 2100. For library preparation, an amount of 2μg of total RNA per sample was processed using Illumina's RNA Sample Prep Kit following the manufacturer's instruction (Illumina, San Diego, CA, USA). In total, we ran 36 samples from three donors. Libraries were sequenced using Illumina HiSeq4000 sequencing platform (Illumina, San Diego, CA, USA) in a paired-end read approach at a read length of 150 nucleotides. Sequence data was extracted in FastQ format. After investigating the quality of the raw data, sequence reads were trimmed to remove possible adapter sequences and nucleotides with poor quality using Trimmomatic v.0.36. The trimmed reads were mapped to the reference genome available on ENSEMBL using the STAR aligner v.2.5.2b. BAM files were generated as a result of this step. Unique gene hit counts were calculated by using feature Counts from the Subread package v.1.5.2. Only unique reads that fell within exon regions were counted. After extraction of gene hit counts, the gene hit counts table was used for downstream differential expression analysis. Differentially expressed genes (DEGs) were identified between conditions using the DESeq2 R package using linear regression.[83] The DESeq and results() functions were used with default parameters to generate DEGs. The results() function has an independent filtering option, which we used for higher statistical power in order to obtain more biologically meaningful results.[84] An adjusted p value cut-off of 0.05 and $|\log_2(\text{fold change})| > \log_2(1.5)$ was also used to obtain biologically relevant results. The results() function also provides Cook's distances, which are helpful for measuring how much a single sample influences the fitted coefficient of a gene.[85] Cook's distances were used to remove outliers from the DEG results. The EnhancedVolcano() function with default parameters from the EnhancedVolcano package version 1.8.0 was used to generate volcano plots of DEGs.[86] Heatmaps of

DEGs, alongside hierarchical clustering of genes and samples, was performed using the pheatmap package with default parameters.[87] Venn diagram of DEGs done online using (http://bioinformatics.psb.ugent.be/webtools/Venn/). A PCA analysis was performed using the "plotPCA" function within the DESeq2 R package. The plot shows the samples in a 2D plane spanned by their first two principal components. The top 500 genes, selected by highest row variance, were used to generate the plot.

### Pathway analysis

Gene Ontology (GO) biological processes, molecular function and cellular compartments and pathway analysis were determined by PANTHER classification system.[32] Functional enrichment analysis was determined using WebGestalt (WEB-based Gene SeT AnaLysis Toolkit).[33] Heatmap of iron metabolism related genes and ferroptosis related genes were generated by Morpheus (https://software.broadinstitute.org/morpheus).

## QUANTIFICATION AND STATISTICAL ANALYSIS

### Data representation and statistical analysis

Statistical analysis was conducted using Graph Pad Prism 9. R package was used for RNASeq analysis. All data are presented as means ± SEM. All cell culture datasets represent means of at least 3 experiments, and the sequence datasets reflect three replicates per condition per donor in three donors. Comparisons between groups were performed using a 2-tailed Student's t test, 1- or two-way ANOVA, as appropriate with appropriate correction for multiple comparisons. Heat maps use $p < 0.05$ for all entities. Statistical parameters can be found in figure legends.

**Cell Reports, Volume *42***

## Supplemental information

# Selective ablation of primary and paracrine senescent cells by targeting iron dyshomeostasis

**Tesfahun Dessale Admasu, Kristie Kim, Michael Rae, Roberto Avelar, Ryan L. Gonciarz, Abdelhadi Rebbaa, João Pedro de Magalhães, Adam R. Renslo, Alexandra Stolzing, and Amit Sharma**

## Supplemental Figures and Tables

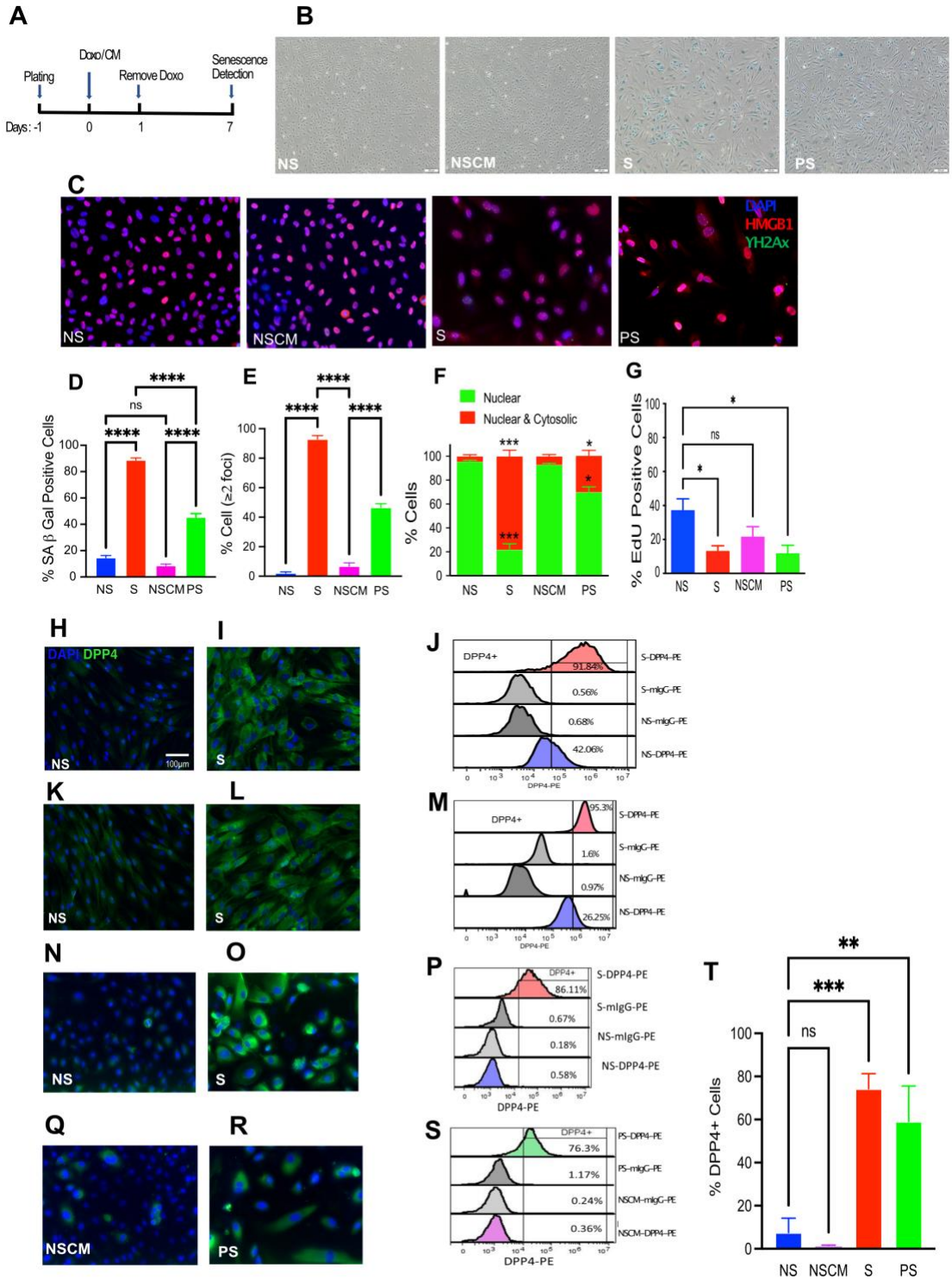

**Figure S1. Related to Figure 1. Primary and paracrine senescent cells express DPP4 on their surface.**

(A) Flow chart of primary and paracrine senescence induction. (B) Representative images of SA β Gal staining. (C) Representative images of γH2AX and HMGB1 immunofluorescence. (D) Percent of SA β Gal positive cells 7 days after doxorubicin or CM treatment. (E) Quantification of γH2AX foci; cells with two or more foci per nucleus were defined as SCs. (F) HMGB1 relocalizes in SCs. Percentage of cells expressing HMGB1 in the nucleus (green) and nucleus + cytosol (red) was scored. (G) Cell proliferation assay, percentage of Click-it EdU Alexa Fluor 488 positive cells. (H-I) DPP4 immunofluorescence staining in fibroblasts (IMR90). (J) Flow cytometry analysis of DPP4 expression in NS and S IMR90. (K and L) DPP4 immunofluorescence staining in mesenchymal stem cells. (M) Flow cytometry analysis of DPP4 expression in mesenchymal stem cells. (N-O) DPP4 immunofluorescence staining of S and NS ECs. (P) Flow cytometry analysis of DPP4 expression in S and NS ECs. (Q-R) DPP4 immunofluorescence staining of PS and NSCM-treated ECs. (S) Flow cytometry analysis of DPP4 expression in PS and NSCM-treated ECs. (T) Percent of $DPP4^+$ ECs from flow analysis in three donors. Values were presented as mean ± SEM. Comparison was made with one-way ANOVA. Error bars = SEM. *P < 0.05, **P < 0.01, ***P < 0.001, ****P < 0.0001.

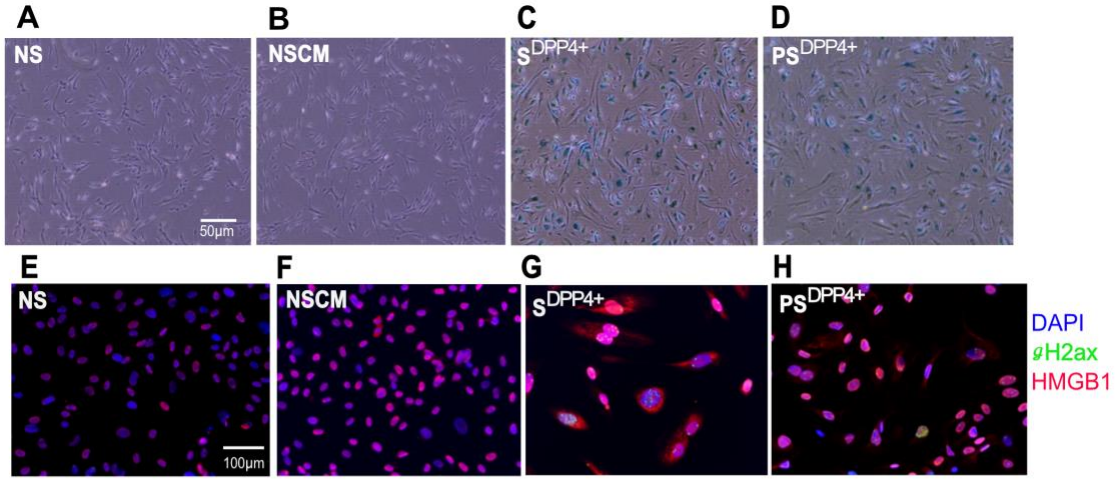
A
B
C
D
NS
NSCM
S^DPP4+
PS^DPP4+
50µm
E
F
G
H
NS
NSCM
S^DPP4+
PS^DPP4+
100µm
DAPI
γH2ax
HMGB1

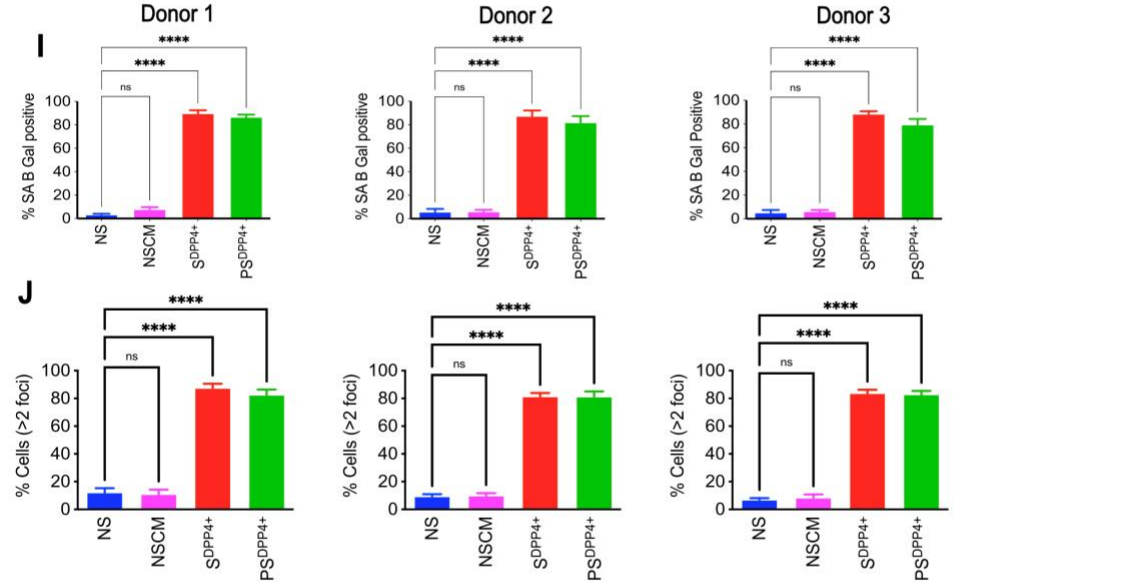
Donor 1
Donor 2
Donor 3
I
% SA B Gal positive
J
% Cells (>2 foci)
NS
NSCM
S^DPP4+
PS^DPP4+
****
ns

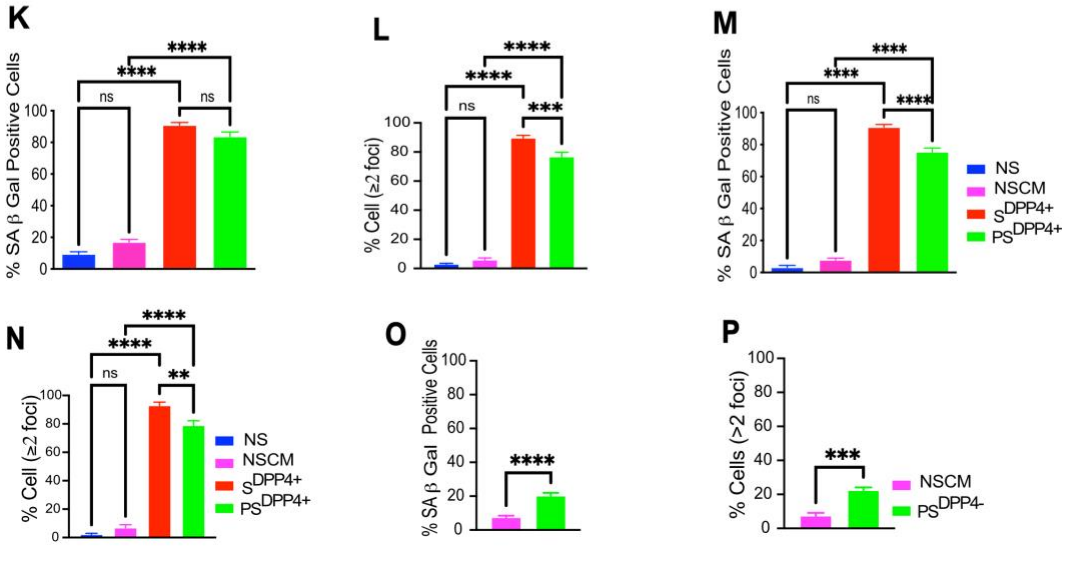
K
% SA β Gal Positive Cells
L
% Cell (≥2 foci)
M
% SA β Gal Positive Cells
NS
NSCM
S^DPP4+
PS^DPP4+
****
***
ns


N
% Cell (≥2 foci)
O
% SA β Gal Positive Cells
P
% Cells (>2 foci)
NS
NSCM
S^DPP4+
PS^DPP4+
PS^DPP4-
****
**
***
ns

**Figure S2. Related to Figure 1. Isolation of live SCs using DPP4 as a surface marker.** (A-D) Representative images of SA β Gal staining in $S^{DPP4+}$ and $PS^{DPP4+}$ and their respective controls. (E-H) Representative images of γH2AX and HMGB1 staining in $S^{DPP4+}$ and $PS^{DPP4+}$ and their NS controls. Both primary and paracrine SCs were isolated based on DPP4 expression and replated. 24hrs after replating cells were stained for SA β Gal, or γH2AX and HMGB1. (I) Percent of SA β Gal positive cells in $S^{DPP4+}$ and $PS^{DPP4+}$ ECs in three donors. (J) Percent of cells with two or more γH2AX foci in $S^{DPP4+}$ and $PS^{DPP4+}$ ECs in three donors. (K) Percent of SA β Gal positive cells in $S^{DPP4+}$ (irradiated) and $PS^{DPP4+}$ ECs treated with CM from irradiated cells. (L) quantification of γH2AX foci in irradiated $S^{DPP4+}$ and their $PS^{DPP4+}$ ECs. (M) as in (K) for doxorubicin treated IMR90 cells and their paracrine SCs. (N) as in (L) for irradiated IMR90 cells and their paracrine SCs. (O) Percent of SA β Gal positive cells in DPP4- flowthrough paracrine senescent ECs. (P) Percent of cells with two or more γH2AX foci in $DPP4^-$ flowthrough paracrine senescent ECs. Values were presented as mean ± SEM. Comparison was made with one-way ANOVA. Error bars = SEM. **P < 0.01, ***P < 0.001, ****P < 0.0001.

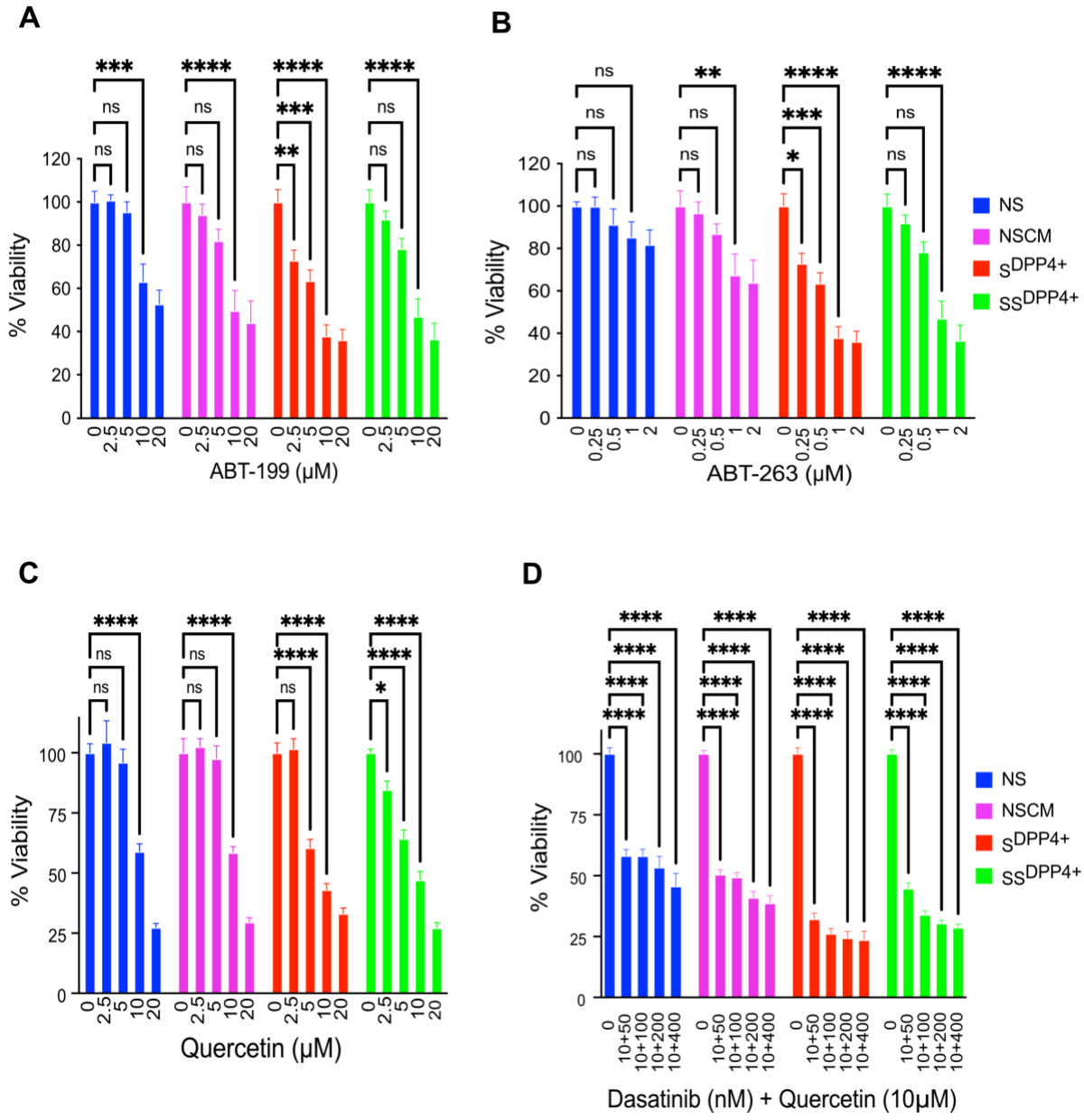
A
B
C
D
% Viability
ABT-199 (μM)
ABT-263 (μM)
Quercetin (μM)
Dasatinib (nM) + Quercetin (10μM)
NS
NSCM
SDPP4+
SSDPP4+
ns
*
**
***
****

**Figure S3. Related to Figure 2. $PS^{DPP4+}$ are refractory to senolytic drugs effective against $S^{DPP4+}$.**

(A) Dose optimization of ABT-199. Viability was determined 24hrs after treatment. The same data with Fig. 2B. (B) As in (A) for ABT-263. Viability was determined 48hrs after treatment. The same data with Fig. 2C. (C) As in (A) for Quercetin. Viability was determined 48hrs after treatment. The same data with Fig. 2D. (D) As in (A) for D + Q combination. Viability was determined 48hrs after treatment. The same data with Fig. 2E. (n=3 technical replicates for 3 donors). Comparison was made with two-way ANOVA. Error bars = mean ± SEM. *P < 0.05, **P < 0.01, ***P < 0.001, ****P < 0.0001.

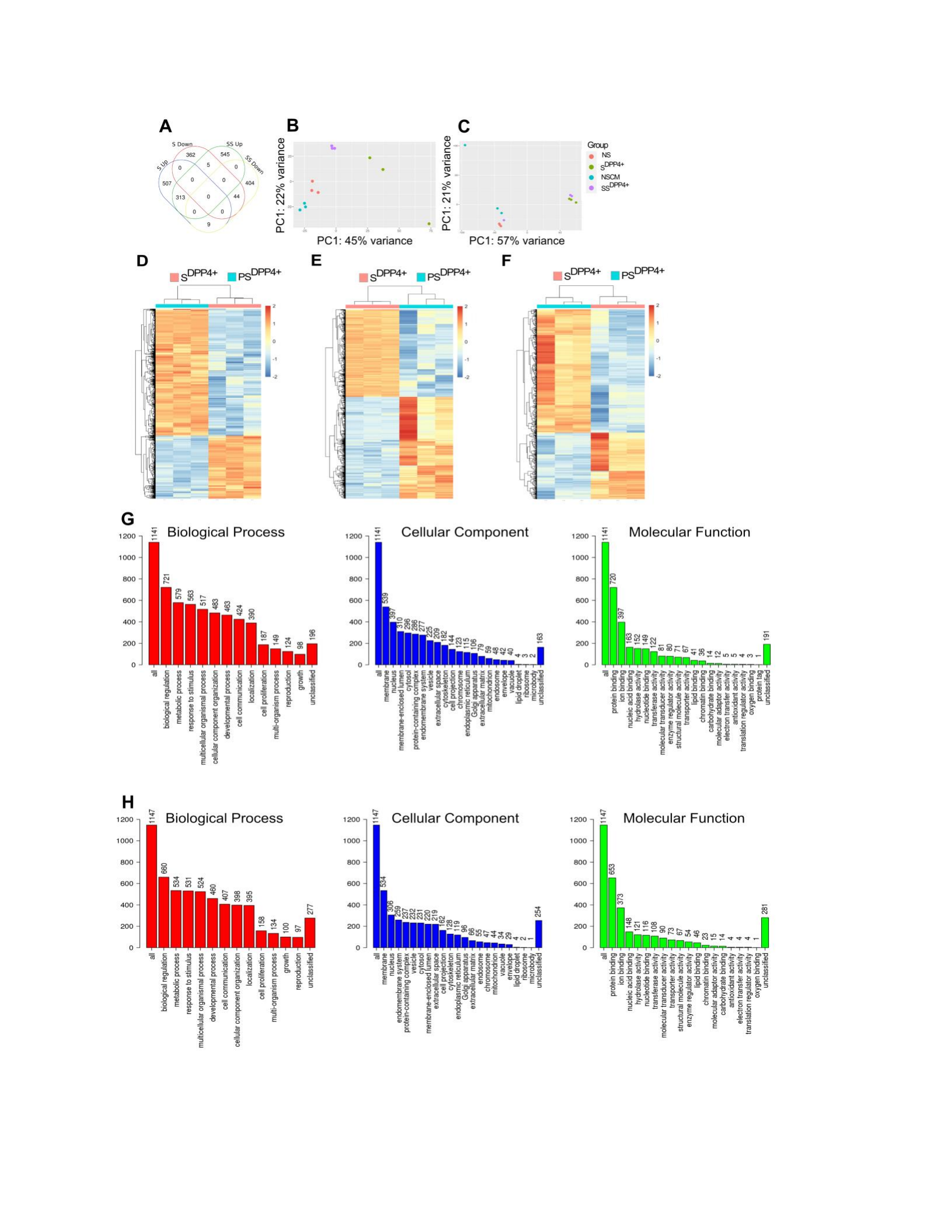
A
S Down
SS Up
S Up
SS Down
362
545
507
404
313
44
9
B
PC1: 22% variance
PC1: 45% variance
C
PC1: 21% variance
PC1: 57% variance
Group
NS
SDPP4+
NSCM
SSDPP4+
D
E
F
SDPP4+
PSDPP4+
G
Biological Process
Cellular Component
Molecular Function
all
biological regulation
metabolic process
response to stimulus
multicellular organismal process
cellular component organization
developmental process
cell communication
localization
cell proliferation
multi-organism process
reproduction
growth
unclassified
membrane
nucleus
membrane-enclosed lumen
cytosol
protein-containing complex
endomembrane system
vesicle
extracellular space
cytoskeleton
cell projection
chromosome
endoplasmic reticulum
Golgi apparatus
extracellular matrix
mitochondrion
endosome
envelope
vacuole
lipid droplet
ribosome
microbody
protein binding
ion binding
nucleic acid binding
hydrolase activity
nucleotide binding
transferase activity
molecular transducer activity
enzyme regulator activity
structural molecule activity
transporter activity
lipid binding
chromatin binding
carbohydrate binding
molecular adaptor activity
electron transfer activity
antioxidant activity
translation regulator activity
oxygen binding
protein tag
H
Biological Process
Cellular Component
Molecular Function

**Figure S4. Related to Figure 3. Transcriptome profile of $S^{DPP4+}$ and $PS^{DPP4+}$.**

(A) Venn diagram of DEGs of $S^{DPP4+}$ and $PS^{DPP4+}$. (B) 2D PCA of $S^{DPP4+}$ and $PS^{DPP4+}$ and NS controls from one donor. $PS^{DPP4+}$ samples were well separated from $S^{DPP4+}$, NS and NSCM-treated samples. (C) 2D PCA of $S^{DPP4+}$ and $PS^{DPP4+}$ and NS and NSCM-treated controls from one donor. $PS^{DPP4+}$ samples were well separated from $S^{DPP4+}$, NS and NSCM-treated samples. (D-F) Heat map of the DEGs for $S^{DPP4+}$ and $PS^{DPP4+}$ for three donors. In each donor $PS^{DPP4+}$ were well separated from $S^{DPP4+}$ and clustered together. Heat maps indicate the averages of 3 experiments (n=3 technical replicates for each 3 donors). (G and H) GO term categories using PANTHER classification system for $S^{DPP4+}$ (G) and $PS^{DPP4+}$ (H). GO terms categorized by biological process, cellular component, and molecular function.

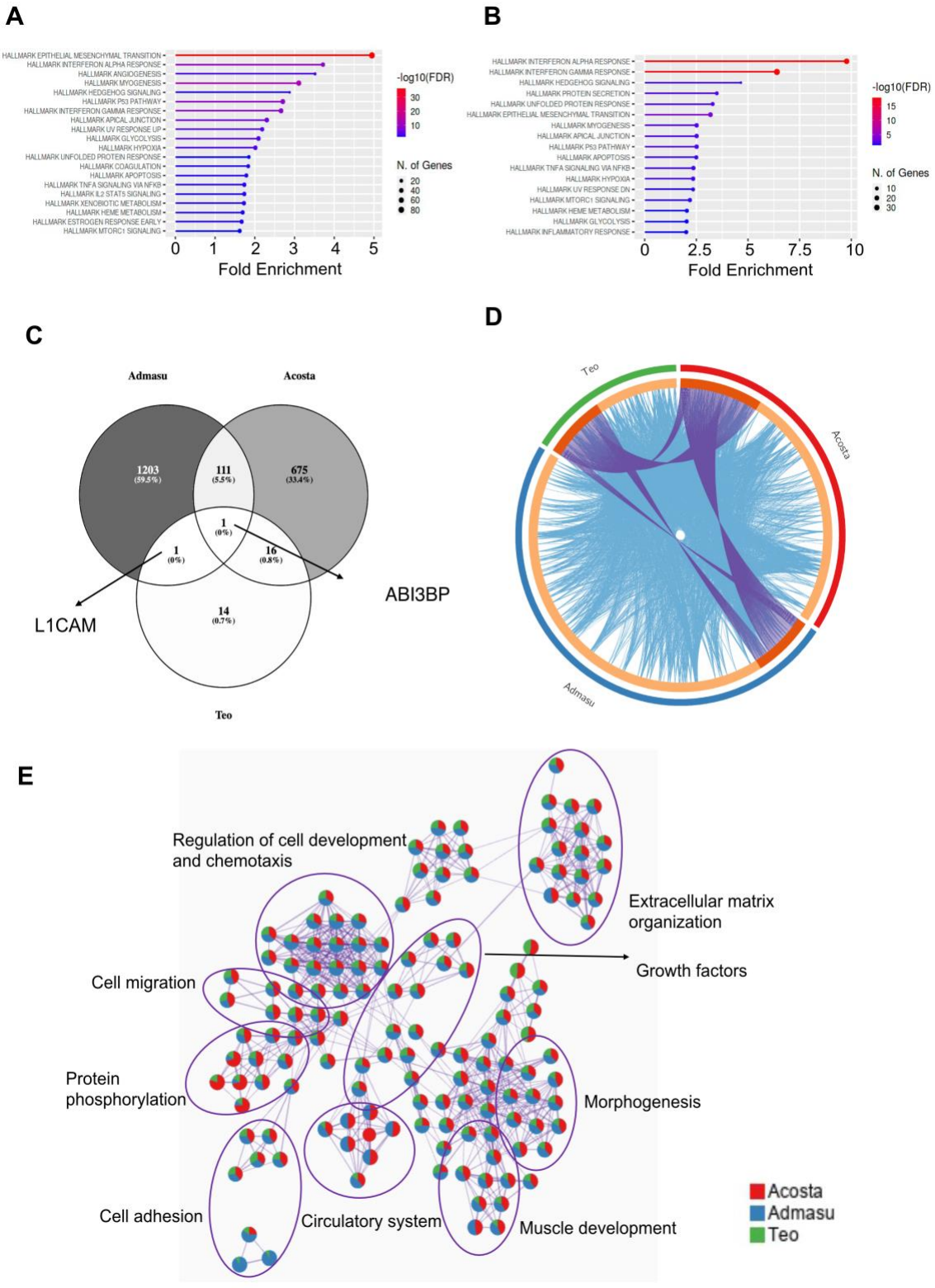
A
HALLMARK EPITHELIAL MESENCHYMAL TRANSITION
HALLMARK INTERFERON ALPHA RESPONSE
HALLMARK ANGIOGENESIS
HALLMARK MYOGENESIS
HALLMARK HEDGEHOG SIGNALING
HALLMARK P53 PATHWAY
HALLMARK INTERFERON GAMMA RESPONSE
HALLMARK APICAL JUNCTION
HALLMARK UV RESPONSE UP
HALLMARK GLYCOLYSIS
HALLMARK HYPOXIA
HALLMARK UNFOLDED PROTEIN RESPONSE
HALLMARK COAGULATION
HALLMARK APOPTOSIS
HALLMARK TNFA SIGNALING VIA NFKB
HALLMARK IL2 STAT5 SIGNALING
HALLMARK XENOBIOTIC METABOLISM
HALLMARK HEME METABOLISM
HALLMARK ESTROGEN RESPONSE EARLY
HALLMARK MTORC1 SIGNALING
0 1 2 3 4 5
Fold Enrichment
-log10(FDR)
30
20
10
N. of Genes
20
40
60
80
B
HALLMARK INTERFERON ALPHA RESPONSE
HALLMARK INTERFERON GAMMA RESPONSE
HALLMARK HEDGEHOG SIGNALING
HALLMARK PROTEIN SECRETION
HALLMARK UNFOLDED PROTEIN RESPONSE
HALLMARK EPITHELIAL MESENCHYMAL TRANSITION
HALLMARK MYOGENESIS
HALLMARK APICAL JUNCTION
HALLMARK P53 PATHWAY
HALLMARK APOPTOSIS
HALLMARK TNFA SIGNALING VIA NFKB
HALLMARK HYPOXIA
HALLMARK UV RESPONSE DN
HALLMARK MTORC1 SIGNALING
HALLMARK HEME METABOLISM
HALLMARK GLYCOLYSIS
HALLMARK INFLAMMATORY RESPONSE
0 2.5 5 7.5 10
Fold Enrichment
-log10(FDR)
15
10
5
N. of Genes
10
20
30
C
Admasu
Acosta
1203
(59.5%)
111
(5.5%)
675
(33.4%)
1
(0%)
1
(0%)
16
(0.8%)
14
(0.7%)
L1CAM
ABI3BP
Teo
D
Teo
Acosta
Admasu
E
Regulation of cell development and chemotaxis
Extracellular matrix organization
Growth factors
Cell migration
Protein phosphorylation
Morphogenesis
Cell adhesion
Circulatory system
Muscle development
Acosta
Admasu
Teo

**Figure S5. Related to Figure 3. Transcriptome profile of $PS^{DPP4+}$.**

(A and B) Functional enrichment analysis using WebGestalt for $S^{DPP4+}$ (A) and $PS^{DPP4+}$ (B). DEG's (|LFC| >= 1, P-value < 0.05) was used as an input for GO term analysis. P-value < 0.05, term enrichment > 1.5 were used as a cut of for the GO terms analysis. (C) comparison of the DEGs of $PS^{DPP4+}$ with previously reported DEGs of secondary SCs. (D) Circos plot illustrating overlap of genes differentially expressed in $PS^{DPP4+}$ and previously reported genes by other groups. Purple lines link genes whose transcription is affected by multiple groups. Blue lines link genes affected by one group only, but which fall into the same GO term. A greater number of purple and blue links and longer dark orange perimeter arcs indicate greater overlap between the DEG and GO terms affected. (E) Enrichment network analysis: each term is represented by a circle node, where its size is proportional to the number of input genes fall into that term, and each pie sector is proportional to the number of hits originated from a group. (Parameters: minimum overlap = 3, minimum enrichment = 1.5, p value < 0.01).

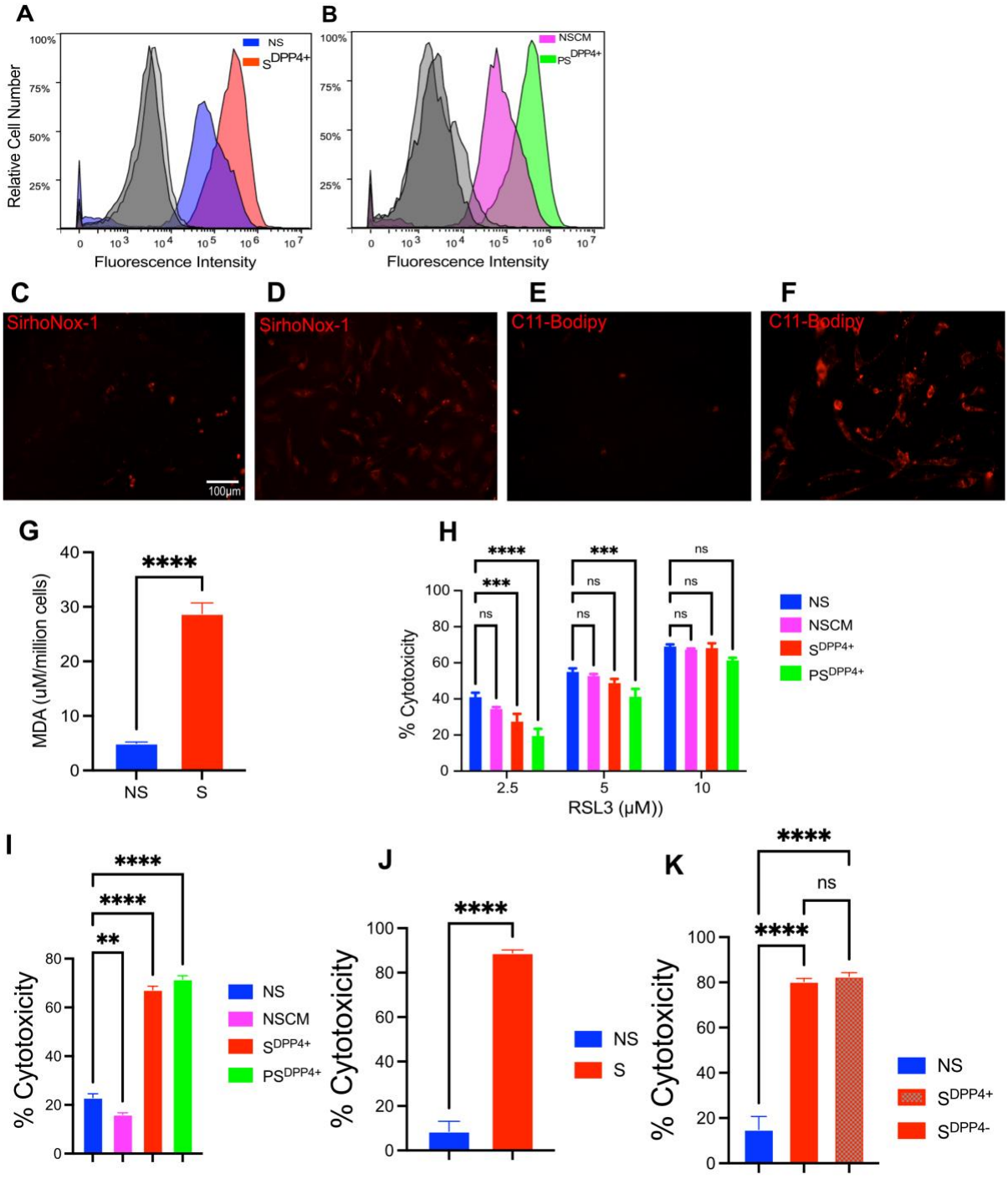
A
B
Relative Cell Number
100%
75%
50%
25%
NS
S^DPP4+
NSCM
PS^DPP4+
0
10^3
10^4
10^5
10^6
10^7
Fluorescence Intensity
C
D
E
F
SirhoNox-1
SirhoNox-1
C11-Bodipy
C11-Bodipy
100µm
G
MDA (uM/million cells)
40
30
20
10
0
****
NS
S
H
% Cytotoxicity
100
80
60
40
20
0
****
***
ns
2.5
5
10
RSL3 (µM))
NS
NSCM
S^DPP4+
PS^DPP4+
I
% Cytotoxicity
****
****
**
NS
NSCM
S^DPP4+
PS^DPP4+
J
% Cytotoxicity
****
NS
S
K
% Cytotoxicity
****
ns
****
NS
S^DPP4+
S^DPP4-

**Figure S6. Related to Figure 4-6. Senescent cells have high ferrous iron content and primed to ferroptosis.**

(A and B) ferrous iron staining using SiRhoNox-1 in $S^{DPP4+}$ (A) and $PS^{DPP4+}$ ECs (B). (C-D) Representative SiRhoNox-1 based ferrous iron staining in NS (C) and S ECs (D). (E-F) Oxidized lipid staining using C11 Bodipy in NS (E) and S ECs (F). (G) Malondialdehyde (MDA) level in S and NS ECs. (H) Cytotoxicity of RSL3 in in $S^{DPP4+}$ and $PS^{DPP4+}$ ECs. (I) Cytotoxicity of FIN56 in etoposide treated $S^{DPP4+}$ and their $PS^{DPP4+}$ ECs. (J) Cytotoxicity of FIN56 in etoposide treated IMR90 primary SCs. (K) Cytotoxicity of FIN56 in in $S^{DPP4+}$ and $S^{DPP4-}$ IMR90 cells.

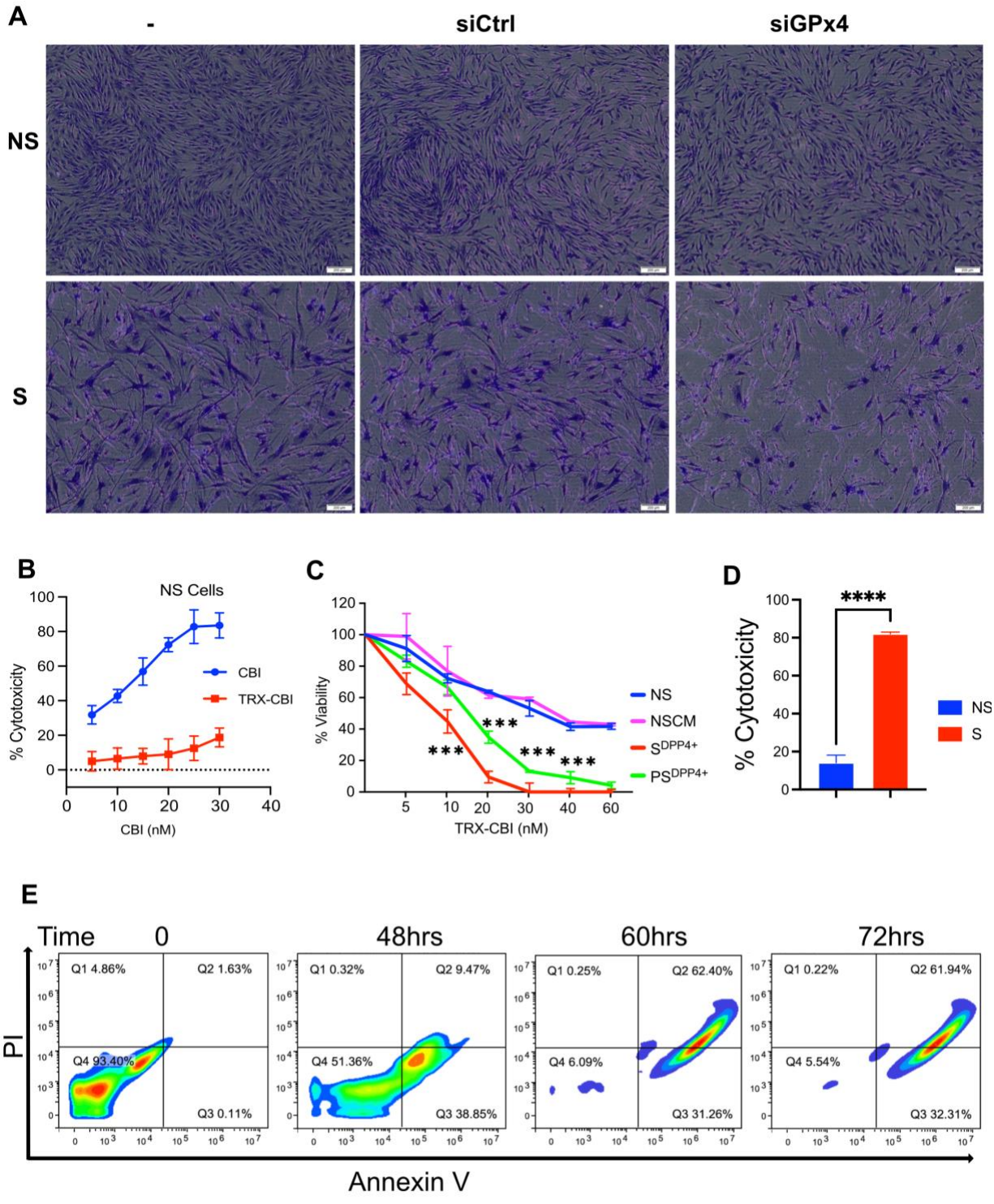
A
-
siCtrl
siGPx4
NS
S
B
NS Cells
% Cytotoxicity
CBI
TRX-CBI
CBI (nM)
C
% Viability
NS
NSCM
S^DPP4+
PS^DPP4+
TRX-CBI (nM)
***
D
% Cytotoxicity
****
NS
S
E
Time
0
48hrs
60hrs
72hrs
PI
Annexin V
Q1 4.86%
Q2 1.63%
Q4 93.40%
Q3 0.11%
Q1 0.32%
Q2 9.47%
Q4 51.36%
Q3 38.85%
Q1 0.25%
Q2 62.40%
Q4 6.09%
Q3 31.26%
Q1 0.22%
Q2 61.94%
Q4 5.54%
Q3 32.31%

**Figure S7. Related to Figure 6. Ferrous iron-activatable prodrug as a senolytic approach**.
(A) Cytotoxicity of CBI and TRX-CBI in NS ECs. (B) Cytotoxicity of TRX-CBI in $S^{DPP4+}$ and $PS^{DPP4+}$ IMR90 cells. (C) Cytotoxicity of TRX-CBI in etoposide treated senescent IMR90 cells. (D) TRX-CBI induces apoptosis in senescent ECs. SCs were treated with 20nM TRX-CBI and apoptosis were determined by annexin V and PI flow analysis at different time point.